UNIVERSITÀ
DEGLI STUDI
DI PADOVA

UNIVERSITA' DEGLI STUDI DI PADOVA

Dipartimento di Ingegneria Industriale DII

Corso di Laurea in Ingegneria dei Materiali

TESI DI LAUREA

EFFECT OF STACKING FAULT ENERGY ON THE MECHANISM OF PLASTIC DEFORMATION IN STEEL AND CUZN ALLOYS

Relatori: Prof.ssa Irene Calliari

Prof. Mészáros István

Laureando: Marco Santacroce

N. matricola: 2016582

Anno Accademico 2022/2023

Summary

INTRODUCTION

The Stacking Fault Energy (SFE) is a characteristic of crystalline materials, associated to the area of stacking faults defects formed in the lattice, that plays an important role for their mechanisms of deformation.

In fact, different values of this parameter can lead to a deformation process mainly controlled by dislocation guide, twinning or martensitic transformation.

In particular, high values of SFE are associated to a cross-slip dislocation mechanism, while in low SFE materials it's favoured the mechanical twinning or, at even lower SFE, martensitic transformation.

Generally, the two principal parameters that influence the value of the stacking fault energy are the chemical composition of the alloy and the temperature.

Understanding the effect of these factors can lead to promising ways to achieve increase in the mechanical properties (especially the strain hardening behaviour) of metals, designating alloys with the desired SFE in order to promote certain deformation mechanism.

In this study samples of three different materials (AISI 304 austenitic stainless steel, pure copper and CuZn alloys with different composition) were used to investigate the correlation between the deformation temperature and the composition with the Stacking Fault Energy.

Specifically, the samples were rolled at several deformation levels under three different temperature conditions: at 100°C, at room temperature and in liquid nitrogen (~77 K).

Successively, the copper and CuZn alloys were investigated using an optical microscope to detect the formation of twinning in the microstructure, while the samples of the stainless steels were tested trough a hardness test and a magnetic investigation to understand the content of the strain induced martensite formed in the austenitic matrix.

All the analyses were carried out at the BME University of Budapest.

CHAPTER 1
Stacking Fault Energy

In metals the stacking fault energy (SFE) is believed to play a critical role in determining which deformation and/or transformation mechanisms will occur during plastic deformation. Consequently, the SFE can to a large extent affect the mechanical behaviour and mechanical properties of these materials.

1.1 Definition of Stacking Fault Energy in FCC structures

In face centered cubic (FCC) structures the atoms are arranged in successive and regular superimpositions of planes at maximum atomic densification in the sequence ABCABC…, as shown in Figure 1.1.

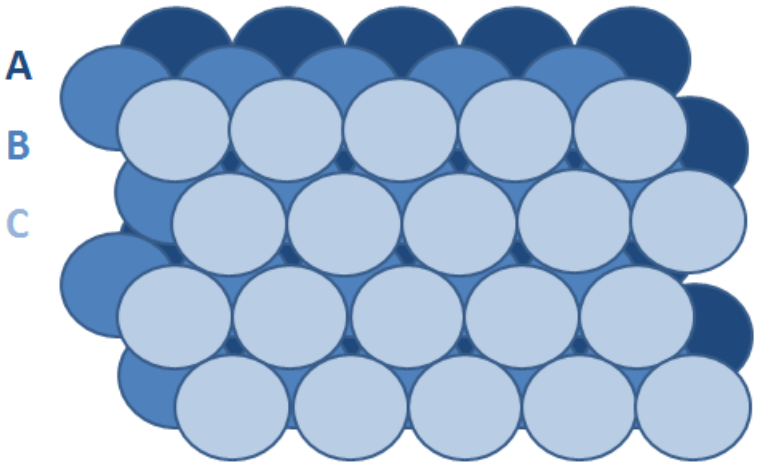

Figure 1.1 *Atomic planes in face centered cubic (FCC) structure.*

In FCC crystals, slip occurs on close-packed (111) planes in <110> directions. The slip of dislocations in such slip systems will leave behind a perfect FCC lattice and are hence called *perfect dislocations*, but in these alloys perfect dislocations often dissociate into two partial dislocations, for which the slip direction instead is <112>. When a single partial dislocation, also referred to as

a *Shockley partial*, passes through the crystal, it creates a region in which the normal stacking sequence is faulted. This faulted region is called a stacking fault (SF).

The atoms of the stacking fault in FCC have an HCP arrangement and, since this is not the equilibrium structure, the SF increases the total energy of the lattice, due to the distortion of atomic bonds and can vary significantly from one material to another.

The energy per unit area of the fault is called *Stacking Fault Energy* and it determines the area of the fault, i.e. the separation distance between the partial dislocations. The equilibrium separation distance *d* is the balance between repulsive and attractive forces between the partials. The repulsive force is due to the partials elastic interaction which will push them away from each other, but since the HCP structure of the faulted area has a higher energy than the normal FCC lattice, the partial dislocations are prevented from splitting too far apart.

The equilibrium width of the SF is inversely proportional to the SFE, which means that a wide faulted area will be created in alloys with low SFE and vice versa

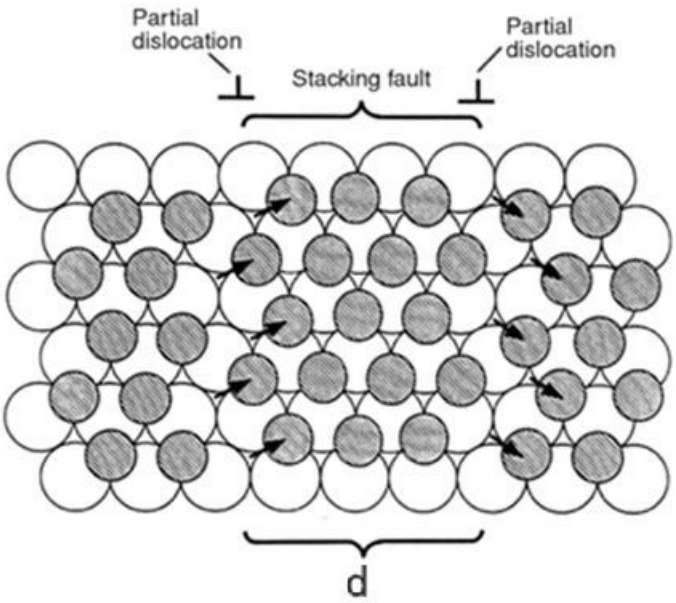

Figure 1.2 *Stacking Fault created by partial dislocations in the lattice.*

The stacking sequence can be altered in two different ways, by eliminating or adding a plane.

As represented in Figure 1.3, when the perfect dislocation slips in the lattice the B atoms are moved along vector (a/2) [110], still remaining in B position after passage. However, an examination of

the slip process reveals that it is energetically favoured for the perfect dislocation to dissociate into two partial dislocations: in fact it is easier for the B atoms to move along a zigzag path in the valleys between the A atoms instead of "climbing over" them. The first partial dislocation with vector (a/6) [211] will move the B atoms into C position, which will produce a defect crystal containing a SF with the stacking sequence ABCACABC…., appearing as if the B layer has been removed from the stacking sequence. The correct stacking of the FCC lattice will not be restored until the second partial dislocation passes. Thus, the partial dislocations represent the boundary that separates the stacking fault from the perfect lattice.

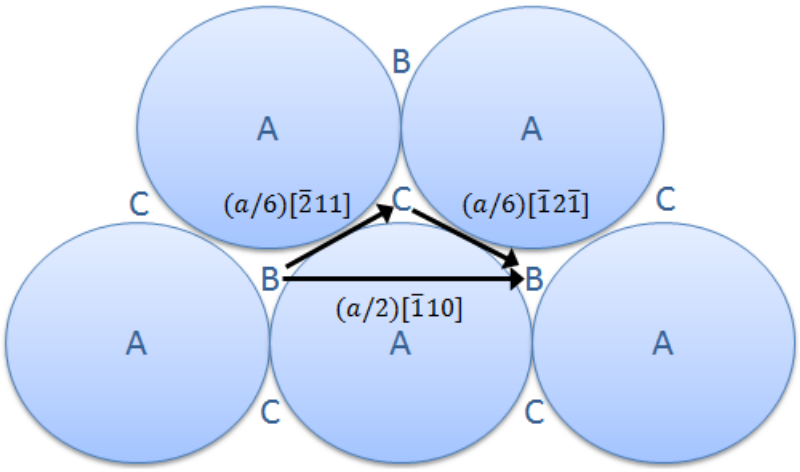

Figure 1.3 *Illustration of the FCC lattice where the slip of a perfect and a partial dislocation is represented by arrows.*

The fault described above, i.e. with the stacking sequence ABCACABC..., that is created by the passage of a single Shockley partial is called *intrinsic*. An intrinsic SF is considered to consist of two planes of hexagonal close packed (HCP) structure.

Instead, the second type of stacking fault defined in the literature, the so called *extrinsic SF* or *twin SF,* has a stacking sequence of ABCACBCAB… and it appears as if an additional C layer has been inserted in the FCC lattice, which produces a twin with the stacking sequence ACB. The extrinsic SF is created by the passage of single Shockley partials on two consecutive planes. The first layer of atoms will be moved from B to C position, as described above, but the consecutive layer will be moved from C to B position when the next single Shockley partial passes. In Figure 1.4, the stacking sequence for a perfect FCC lattice is compared to the stacking sequence of an intrinsic and extrinsic SF. [4] [11] [12][13]

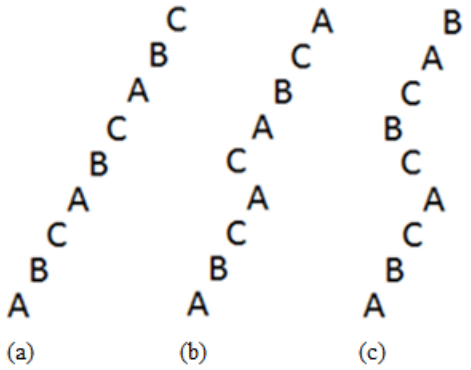

Figure 1.4 *Stacking sequence for a (a) perfect FCC lattice, (b) intrinsic SF and (c) extrinsic SF.*

1.2 Effect of the SFE on the mechanisms of deformation

Dictated by the chemical composition and the deformation temperature, the stacking fault energy controls the deformation accommodation mode as shown schematically in Figure 1.5.

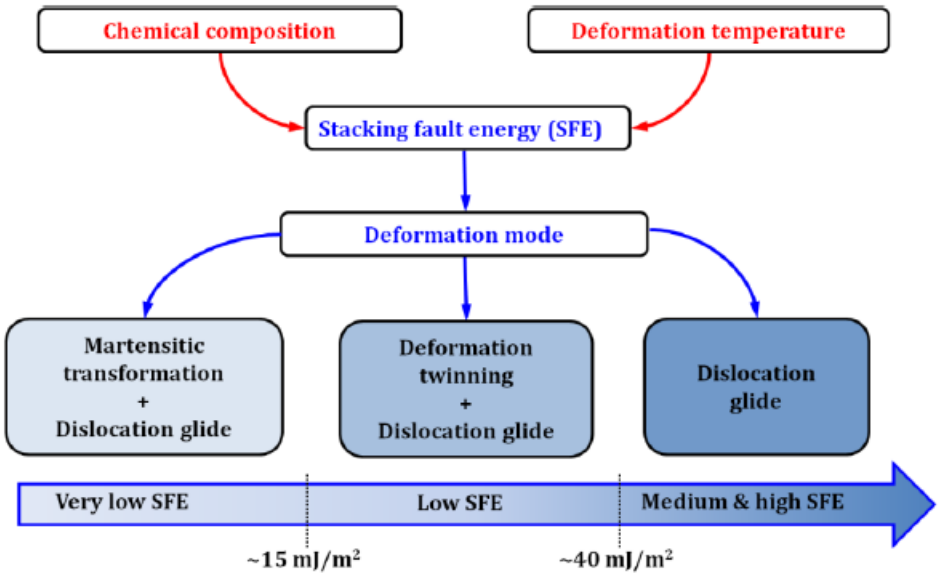

Figure 1.5 *Dependence of deformation modes on stacking fault energy.*

In the high SFE case dislocations are rarely dissociated, thus the deformation process is controlled mainly by dislocation glide of perfect and partial dislocations which can accumulate into slip band; instead, in materials with low SFE, wide partial dislocations will hinder dislocation glide and favour mechanical twinning or at even lower SFE, martensitic transformation. Since the SFE depends on chemical composition, alloys with the desired SFE can be designed in order to promote certain deformation mechanisms.

In fact, SFE determines the width of the stacking fault of dissociated dislocations: higher SFE results in a smaller separation between partials and facilitates cross-slip, while in low SFE materials the large separation between partial dislocations inhibits this deformation mechanism. Therefore, in this last case, dislocations are confined to major slip planes and it's favoured the deformation by twinning.

In particular, twinning is reported to occur at SFE's roughly between 15-40 mJ/m^2. At lower values martensitic transformation is favoured and when the SFE exceeds about 40 mJ/m^2, the deformation process is only controlled by the glide of dislocations.

To this end, the stacking fault energy not only influences the deformation modes and the associated hardening behaviour but also dictates the evolution of crystallographic texture during any deformation or annealing process.

Tailoring plastic deformation mechanisms has been proven to be one of the most promising routes to achieve increases in strain hardening and ductility, in particular design approaches based on metastability including transformation induced plasticity and twinning induced plasticity effects.

From the microstructure evolution of the CuZn alloys it's possible to observe different features that are characteristic of both high and low-SFE materials: dislocation regions which tend to transform into equiaxed cell-like structures as the strain increases (*copper-type regions*) and regions containing deformation twins (*brass-type regions*). Specifically, this difference in the microstructure is evident in materials with notably different SFE, starting from the pure copper (high SFE) and increasing the content of Zn in the alloy (and consequently decreasing the SFE), where it's possible to detect dislocations organised in cell structures or, with a lower SFE, in planar arrays (or a mixed microstructural structure between the two as in CuZn15) and finally twin boundaries.

On the other hand, taking austenitic steels as example, it's possible to investigate the two competitive deformation mechanisms to dislocation glide: twinning and ε martensite (HCP) transformation.

The HCP structure is formed by the motion of single Shockley partials on every second close-packed plane, that is to say formation of intrinsic SF's on every second plane. By the same principle the twin structure is formed by the motion of Shockley partials, but here instead on neighbouring planes. When comparing the formation of the HCP and twin structures, it is obvious that the formation mechanisms for the two structures are very similar. In fact, both structures can be observed within the same shear bands and the mechanisms are clearly correlated through the concept of stacking fault energy

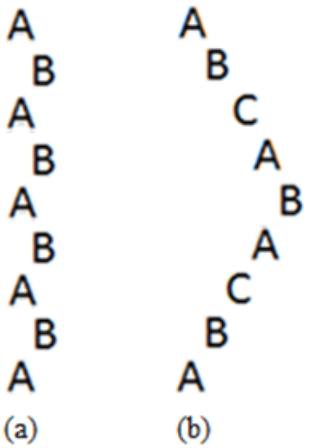

Figure 1.6 *Stacking sequence for the (a) HCP structure and (b) twin structure.*

The two principal parameters that influence the value of the stacking fault energy are the chemical composition of the alloy and the deformation temperature.

For the first one many empirical relationships have been proposed over the years, however the empirical formulas are limited to certain composition ranges and temperatures and fail in reproducing the compositions nonlinear effect on the SFE.

Several studies investigate different alloying elements effect on the SFE and some alloying elements seem to have a clear effect on the SFE while some others seem to have a more complex relationship.

In general, the details of the composition influence from alloying elements on the SFE are not easy and need to be investigated closely in each case on order to be fully understood.

The same alloying element can cause opposite changes in the SFE with different host composition (Ni and Cr raise the SFE in Fe-Mn alloys but have the inverse effect for carbon steels) and at the moment there are no universal composition equations for the SFE.

Instead for the temperature it seems clear that it strongly affects the stacking fault energy, specifically an increased temperature gives an increased value of SFE. [11] [12] [13] [33] [37] [40]

1.2.1 Twinning

The sliding is not the only type of deformation that can be had in crystals: in fact, if the interplanar movements are hindered, they can deform for twinning.

The competition between slip and twinning is a key phenomenon governing the plastic deformation of many metals and alloys with FCC structure.

Conventionally, the consensus has been that the deformation twinning is favoured in metals like gold and silver, which have low stacking fault energies.

Also, several FCC alloys like Cu-Al alloys and Twinning Induced Plasticity (TWIP) steels exhibit twinning during deformation at room temperature.

As a result of this process, some atoms of the crystals, when sheared, change their arrangement so that they become mirror images of others with respect to the twinning plane.

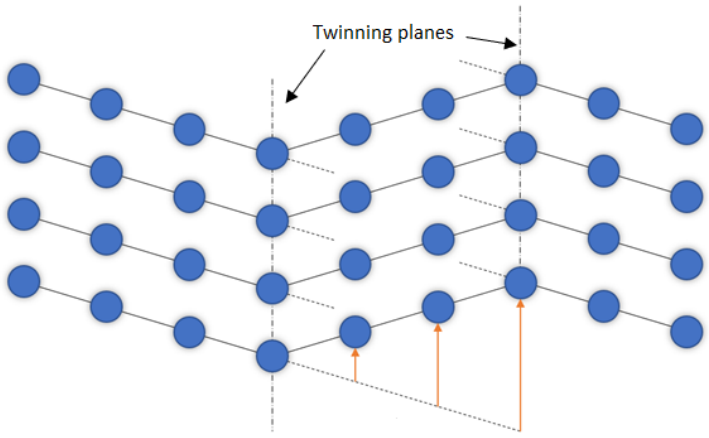

Figure 1.7 *Atomic configuration in twinning.*

Each atomic plane moves in the same direction as an amount proportional to its distance from that of twinning, which can be considered an almost perfect joint and its trace represents the axis of symmetry.

In fact, the twin always contains a certain number of dislocations to accommodate on the other sides the consistency with the matrix; this implies that the energy required for its formation is higher than that needed to begin the sliding.

In metals with FCC grating twinning can be favoured by high stresses and the presence of impurities that, especially if interstitial, create tensions that raise the sliding threshold.

With respect to the deformation by sliding, in the deformation by twinning there are opposite parts of the plane with different crystalline orientations, the atomic movements are little extended (much smaller than an interatomic distance) and involves all the plans of the region concerned.

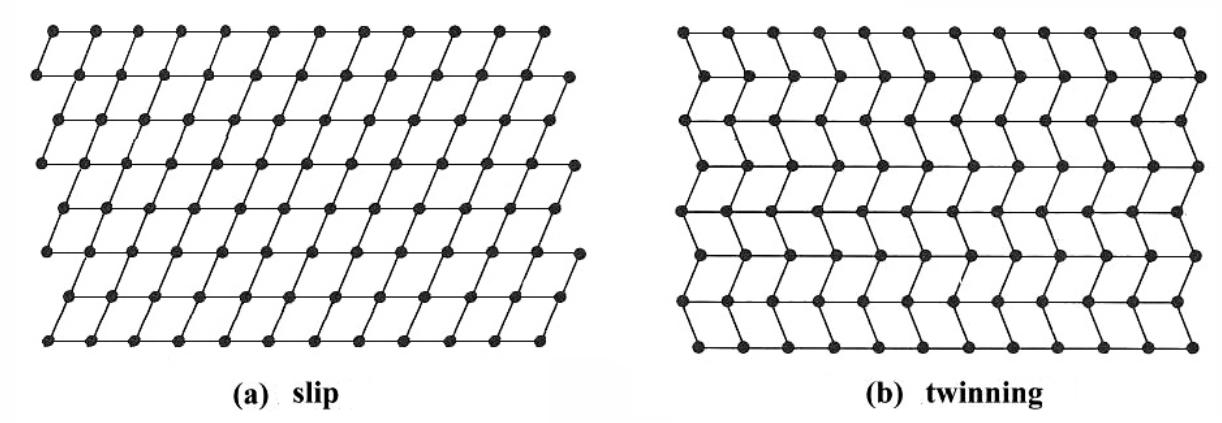

Figure 1.8 *Difference in the structure obtained after (a) slip and (b) twinning.*

The nucleation of mechanical twins is critically dependent upon the grain size, the amount pf pre-strain and the stress condition of the material prior to its deformation.

The deformation mechanism closely depends on the SFE of the metals: in the case of low SFE the partial dislocations that constitute a glide dislocation are more widely separated or extended than in higher SFE materials.

Thus, the stacking faults between the partials must first be compressed by a high stress to overcome the repulsive forces between the partial dislocations; therefore, cross slip is suppressed and the deformation tends to be planar.

Simultaneously, under stress, a perfect (110) dislocation in a FCC lattice usually dissociates into two Shockey partials connected via an intrinsic stacking fault defect for energetic reasons: double partials dislocation glides on the same plane may not be possible it forms a high energy stacking sequence, while single partial dislocation glide on each plane is more energetically favourable.
The stacking faults are more preferential to overlap and glide successively on adjacent slip planes. This process has been found to initiate deformation twinning.
Once a twin is formed by dislocation interactions, it may be thickened by overlapping of other nuclei formed on the (111) planes parallel to its habit plane and this is why the density of twins increases with increasing strain.
In FCC alloys with low SFE, where deformation twinning is supposed to play a key role, recent studies show that twins have a remarkable effect on the mechanical properties. In fact, for these materials the twin boundaries frequently observed during plastic deformation can strengthen the alloy more efficiently, in contrast to dislocation accumulation.
Thus, twin boundaries can impede the dislocation movement, subdividing the grains into twinned and untwinned regions, and inducing a significant increase in strength. In these cases, the experimentally observed Hall-Petch slope for twinning is higher than that for dislocation slip and, therefore, the materials always show a higher strain hardening rate.
Specifically, FCC alloys such as brass, nickel alloys, austenitic steel and non-FCC alloys such as titanium alloys are reported to have relatively higher strain hardening rates and high ductilities attributed to deformation twinning, making them important commercially for a number of structural reasons. [4] [33] [39] [40] [41] [42]

1.2.2 Strain Induced Martensite

Martensite is an oversaturated solution of carbon, whose transformation occurs almost instantaneously due to the impossibility of diffusive phenomena both by carbon and by iron.
The transformation then takes place through a coordinated movement of the atoms, and therefore not diffusive, without altering the composition of the starting austenite.
Because of their large concentration in alloying elements, austenitic stainless steel has a very low Ms temperature and therefore do not generally form martensite, but sometimes this structure can be obtained with the aid of plastic strain.

In fact, many work clearly showed that the austenitic phase in AISI 304 stainless steels is metastable. Consequently, this phase can be transformed to alpha prime martensite (α') and epsilon martensite (ε) also above Ms, when an additional driving force is provided by an applied load.
This strain induced martensitic transformation occurs after the yield point, where the effect of stress and strain generate potent nucleation sites to lower the barrier of transformation.
The martensite transformation can be developed during the manufacture process, such as machining, forming and welding, and/or as a result of loading during component operation.
In particular, at very low stacking fault energy values (<15 mJ/m^2), the austenite phase is unstable such that it transforms to martensite during room temperature deformation. Phase transformation occurs to either hexagonal close packed (HCP) ε martensite "$\gamma \rightarrow \varepsilon$" or, body centered cubic (BCC) α' martensite. The latter is promoted by lower values of stacking fault energy or at higher strains and can occur via two possible routes: $\gamma \rightarrow \alpha'$ or $\gamma \rightarrow \varepsilon \rightarrow \alpha'$.
The structures of the two types of martensite are shown in Figure 1.19.
The ε-martensite forms on close packed (111) planes in the austenite with crystal structure, while the α' martensite forms as plates with (225) habit planes in groups bounded by faulted sheets of austenite on (111) planes stainless steels.
The α'-martensite is thermodynamically much more stable than the ε phase; epsilon martensite form before during cold rolling but at higher deformations the α' phase grows at the expanse of the previously formed martensite, causing its content decreasing. It was found that the α'-phase is formed almost exclusively at the intersection of twin faults or shear bands (bands of imperfect micro twins), stacking faults and ε-phase (so from locations where the stress is highly concentrated).
Strain induced martensite formation is dependent on various factors, i.e chemical composition, temperature, degree of plastic strain, grain size, strain and stress state.
In particular, the composition determines the stability of austenite: for example, nickel increases the stacking fault energy and, therefore, it decreases the formation of martensite.
It's important to notice that the lattice transformation from FCC to BCC in austenitic steels drastically changes their magnetic properties: austenite is a paramagnetic phase (as the HCP epsilon martensite), in contrast to strain induced martensite α', which is strongly ferromagnetic.
For this reason, the transformation from austenite to martensite represents a significant alteration of the magnetism of a body. [5] [14] [28] [30] [31] [32] [38]

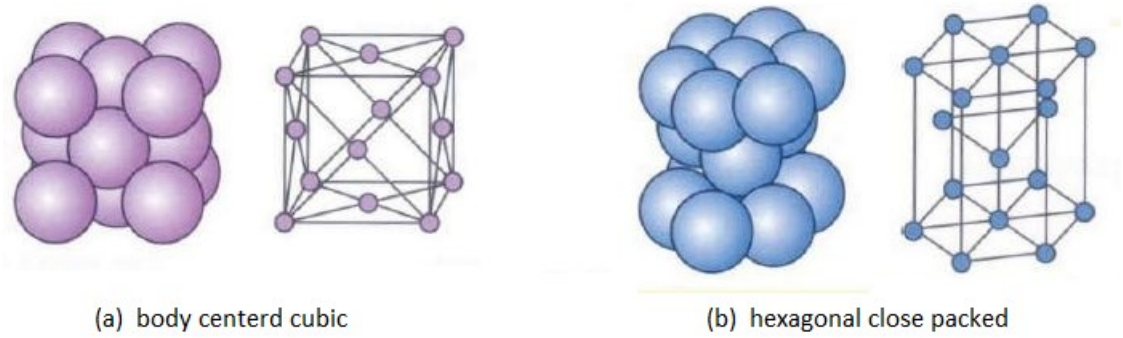

Figure 1.9 *Lattice structure of (a) α' martensite and (b) ε martensite.*

CHAPTER 2
Stainless steels, Copper and CuZn alloys

2.1 Stainless steels

Stainless steels are alloys of iron with chromium, nickel, and, often, other elements (Mo, Cu, S, Nb...), in order to obtain desired properties.

Although they represent only 2% of the production, stainless steels are a class of steels highly requested industrially, thanks to their particular attitude for resisting corrosion; therefore, they are used mostly in chemical, food, pharmaceutical, furnishing and household industries, or when unalterable aesthetic qualities are necessary. [3] [25]

2.1.1 General Characteristics

The corrosion resistance of the alloy is guaranteed by the presence of a minimum 12% chromium content, necessary to passivate it; in this case, if the environment is sufficiently oxidizing, a passive oxide film is formed on the surface of the alloy which protects the underlying material.

Most stainless steels are alloys of iron (Fe) with chromium (Cr) and nickel (Ni): the ternary phase diagram, at a temperature of 800° C, for those three elements is shown in Figure 2.1.

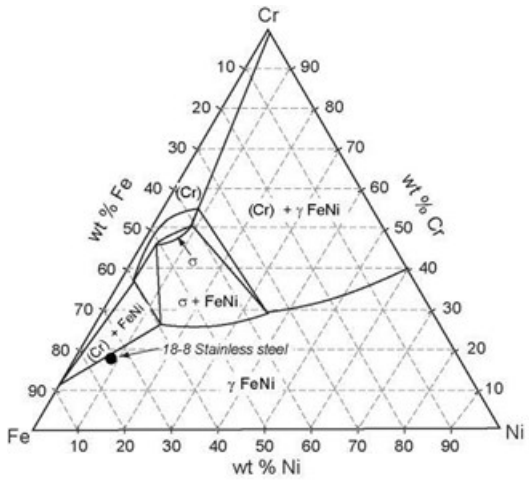

Figure 2.1 *Ternary phase diagram of Fe, Cr and Ni at 800°C.*

Other elements can be added to the alloy in order to enhance some specific characteristics (carbon to give hardness, molybdenum to improve resistance to pitting, titanium and niobium to avoid intercrystalline corrosion, sulphur to increase machinability, etc.).

Summarizing the alloying elements transmute plain carbon steel that rusts and is prone to brittleness below room temperature into a material that is able to resist corrosion in most normal environments and to remain ductile to lower of temperatures.

It's important to remember that stainless steel must be used efficiently to justify its higher costs, exploiting its high strength and corrosion resistance. Surface finish can be controlled by rolling, polishing or blasting.

Stainless steels are selected, first, for their corrosion resistance, second, for their strength and third, for their ease of fabrication; indeed, many stainless steels are difficult to bend, draw and cut, requiring slow cutting speeds and special tool geometry.

They are available in sheet, strip, plate, bar, wire, tubing and pipe, and can be readily soldered and braised. Welding stainless steel is possible but the filler metal must be selected to ensure an equivalent composition to maintain corrosion resistance.

Moreover, stainless steels are FDA approved, indeed they are so inert that they can be implanted in the body and are widely used in food processing equipment. [3] [19] [22] [23] [24]

2.1.2 Designation and Classification

Depending on the microstructure, stainless steels are classified into austenitic, ferritic, martensitic and duplex.

The most common unification for designating stainless steels is the American AISI, which uses three-digit numbers: austenitic steels (Fe-Cr-Ni-Mn or Fe-Cr-Ni) are designated by numbers of the 200 (2xx) or 300 series (3xx), while ferritic (Fe-Cr) and martensitic (Fe-Cr-C) steels belong to the 400 series (4xx).

Other stainless steels (austenitic-ferritic duplex, low interstitials ferritic, precipitation hardening alloys or alloys with higher element contents) are designated with initials chosen by the manufacturer.

- *Austenitic stainless steels*

  From a general point of view, austenitic steels are those that present the best resistance to corrosion, followed by ferritic and martensitic steels.

They usually contain chromium (approximately 18%, in some case up to 25%) and nickel (9-13%), as well as other possible alloying elements depending on the final requests; the amount of carbon is normally under 0.1%.

Austenitic stainless steel with high molybdenum content and copper has excellent resistance to pitting and corrosion, instead high nitrogen content gives higher strength.

It should be remembered that even the most alloyed austenitic stainless steels cannot withstand some highly aggressive environmental conditions; it is then necessary to resort to superalloys (based on nickel, chromium, molybdenum and cobalt).

- *Ferritic stainless steels*

  Ferritic stainless steels contain iron and chromium (11.5-27%) and carbon is also here almost always relegated to the role of impurity (<0.10%).

  The most commonly used type is *AISI 430* steel which nominally contains 17% chromium and 0.08% carbon.

  Chromium contents below 17% increase weldability and impact resistance, but also decrease the corrosion resistance; by increasing the chromium content, the carbon content can also be increased allowing to obtain better mechanical strength characteristics.

  Compared to austenitic they have a lower resistance to corrosion, but have a lower price because they do not contain nickel and are less subject to both stress corrosion and intercrystalline corrosion.

  They are used in the nitric acid industry, such as monetization alloys, etc.

- *Martensitic stainless steels*

  Martensitic stainless steels have a chromium content between 12% and 17%, with the upper limit imposed by the possibility of assuming martensitic structure after quenching.

  These steels are particularly suitable for cases where high mechanical strength characteristics, typical of the martensitic structure, are necessary, associated with a good inertia to corrosion.

  They are quenched from 1000 ºC and subsequently tempered at a temperature that depends on the use for which they are intended: 600-650 °C for mechanical components (turbine blades, valve parts, collectors, shafts, pins and axles for the extractive industry) or 380-400°

C for retaining hardness and for use as tools (cutlery, scissors, surgical or measuring instruments), motor injectors, bearings, etc.

The most commonly used in this class is *AISI 420*, containing Cr=13% and C=0.20%.

Increasing the carbon content increases the mechanical properties of strength and hardness, but at the expense of weldability (already precarious) and ductility.

- *Duplex stainless steels*

  They are more recent than the others stainless steels and, thanks to the adequate dosage of the alloying elements (chromium 22-25%, nickel 4-7%, molybdenum 0-4%, nitrogen 0.1-0.25%) they show a microstructure composed half austenite and half ferrite.

  They have, compared to austenitic steels, better characteristics of mechanical resistance (associated to the nitrogen content) and corrosion under stress.

  The combination of austenitic and ferritic structures also provides considerably slower growth of stress-induced cracks.

  The addition of increasing molybdenum (and nitrogen) contents also increases their inertia to generalized and localized corrosion and, in many applications (particularly in the oil field and in the production of high temperature exchangers), this class of materials is considered a better choice than conventional austenitic steels. [3] [19] [22] [23] [24]

Table 2.1 *Most used stainless steels.*

Steels	**AISI**	**Composition** [%]					R_m [N/mm^2]	R_s [N/mm^2]	**A** [%]	**HR** (B or C)
		C	**Cr**	**Ni**	**Mo**	**N**				
Austenitic	303	0.10	18	9	-	-	650	280	45	B82
	304	0.05	19	9	-	-	506	241	55	B80
	316	0.06	17	12	2.5	-	620	276	50	B79
	304L	0.03	19	10	-	-	517	193	55	B79
	316L	0.03	17	12	2.5	-	517	220	50	B79
Ferritic	430	0.08	17	-	-	-	550	250	18	B82
Martensitic	410	0.12	13	-	-	-	800	500	15	C41
	420	0.20/0.40	13	-	-	-	950	550	10	
	440	0.60/1.20	17	2	-	-	750	430	18	
Duplex	23-04	0.02	18	4	-	0.10	700	400	25	B92
	22-05	0.02	22	5.5	3	0.14	800	450	25	C23
	25-07	0.02	25	7	4	0.25	920	506		

2.1.3 Austenitic stainless steels

These steels represent more than 60% of the total production of stainless steels, as they are the ones that better resist both hot and wet corrosion and therefore are used in all fields in which corrosion behaviour is a priority; they are also very cold deformable.

The prolonged formability of these steels is mainly linked to the FCC lattice and corresponding high potential of multiple slipping systems, which are activated during plastic deformation, avoiding crack creation and rupture.

Their outstanding corrosion, as well as chemical resistance and high formability, makes austenitic stainless steels suitable candidates of components in a variety of applications, like automotive, aerospace and chemical industry.

The stability of austenite at room temperature (or lower) is driven by alloying, i.e, the presence of austenite stabilizers (Ni, C, N, Mn, Cu, Co).

The typical steel of this class is *AISI 304*, also known as *X5CrNi1810* (UNI designation) or more simply 18/10, which still today represents more than a third of the entire stainless steel production. It contains chromium (18-20%) and nickel (8-10.5%), while carbon (<0.06%) is relegated to the role of impurity.

Here the chromium protects by creating a protective Cr_2O_3 film on all exposed surfaces, and the nickel stabilizes face-centered cubic austenite, giving ductility and strength both at high and low temperatures. They are non-magnetic and this represents a way to identify them.

Since the M_s temperature is below room temperature, austenitic stainless steels cannot undergo quench hardening treatments to increase the mechanical characteristics of resistance, but only solubilization of any carbides present to avoid intergranular corrosion, or stress relieving to avoid internal tensions after unwanted cold deformation.

The mechanical characteristics, modest in the solidified state (R_s= 2500 N/mm^2), can only be increased by cold plastic deformation (for example rolling or drawing); moreover, hardening is so strong that they are also used to make stainless springs, quadrupling the breaking strength

Another limitation of these steels is the low resistance to stress corrosion cracking, generated by the combined action of an aggressive environment and tensile stresses.

To achieve specific improvements in the properties of resistance to generalized, localized and intergranular corrosion (but not to stress corrosion cracking), weldability, mechanical

characteristics and workability, some modifications have been made to the basic chemical composition of AISI 304 steel.

Among the most important it should be remembered:

- the addition of small amounts of titanium (*AISI 31*) or niobium (*AISI 347*) in order to obtain the so-called *stabilized steels*, which are less affected by intergranular corrosion.
- the addition of molybdenum in contents of 2-3% (*AISI 316*) to improve corrosion by pitting or crevice corrosion.
- the reduction of the carbon content (*AISI 304L* or *316L*, with C content < 0.03%) in order to almost totally eliminate the possibility of intergranular corrosion, for example in welded structures.
- the addition of sulphur (*AISI 303* and *316F*) to improve chip breaking. [3] [19] [22] [23] [24] [35]

2.2 Copper

Copper has a distinguished place in the history of civilization: it enabled the technology of the Bronze Age (3000 BC - 1000 BC) and in general his knowledge dates back to a few millennia ago, much earlier than the discovery of iron. Now copper is one of the most used metals, employed in many forms: as pure copper, as copper-zinc alloys (brasses), as copper-tin alloys (bronzes), and as copper-nickel and copper-beryllium. [3] [18]

2.2.1 General Characteristics

Copper is easy to cast, to roll to sheet, to draw to wire, and to shape in other ways.

It resists corrosion in the atmosphere, acquiring an attractive green patina (copper carbonate) in clean air, and a black one (copper sulphide) in the other case.

Pure copper has excellent electrical and thermal conductivity (greater than those of any other metal except silver), is easy to fabricate and join, has good corrosion resistance and reasonable strength. The presence of impurities, especially those that enter into a solid solution with it, is associated with a decrease of the conductivity because it causes a reticular distortion that hinders the motion of electrons (where high conductivity is necessary, oxygen-free high-conductivity OFHC copper is used).

Copper has no allotropic transformations and has a FCC structure with a very fine grain: therefore it is very malleable and is preferably worked cold, after which it is almost always subjected to recrystallization annealing, at about 600 ºC, to eliminate work hardening.

When hot, this metal has a remarkable affinity for oxygen and therefore, after casting or remelting, it always contains some Cu_2O (0.5-1%); such low concentrations however do not appreciably affect its mechanical properties.

Moreover, copper is easily weldable, exceptionally durable (copper artifacts 2500 years old survive today) and it is visually attractive: copper objects are prized, and prestige buildings are clad with it.

The main uses of metallic copper are based on its high electrical (in wiring, conductors, cables. busbars, etc.) and thermal (in pipes, heat exchangers, heat sinks, kettles, boilers, etc.) conductivity, as well as its good corrosion resistance. [3] [17] [18] [19]

2.2.2 Designation and Classification

The designation of '*copper*' is used when the percentage of copper is more than 99.3%.

Depending on the preparation methods this metal is distinguished in *refined* (purity 96-99%) and *electrolytic* (purity 99.5-99.99%).

There is now a UNS designation system for copper and its alloys: the letter C (for 'copper') followed by a 5-digit number. Only the first digit means anything: C1**** designates almost pure copper, the C2, C3 and C4 series are brasses with increasing zinc content, the C5s are bronzes based on copper and tin, the C6s are other bronzes containing aluminium instead of tin, and the C7s are copper-nickel alloys. [3] [17] [18] [19]

2.3 CuZn alloys

Metallic copper is not suitable for structural uses due to its very low resistance: from this point of view, indeed, it is one of the softest metals. However, the addition of solid solution elements hardens it (as shown in Figure 2.2), which is attractive for many applications.

The elements that are added most often are zinc, tin, aluminium and nickel.

The alloys thus obtained are of considerable importance from an application point of view, also by virtue of their good resistance to corrosion, which derives from the excellent one of copper.

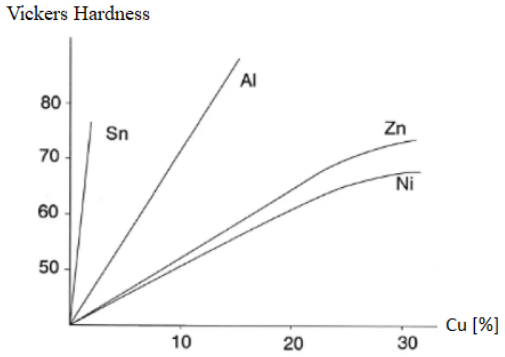

Figure 2.2 *Effect of different alloying elements on the Vickers Hardness of the copper alloy.*

Brasses are alloys of copper (Cu) with 5 - 40% zinc (Zn). They combine excellent formability and machinability with good corrosion resistance. As the zinc content increases the melting point, density, modulus and electrical and thermal conductivities decrease; instead. the expansion coefficient, the strength and the hardness increase. [3]

2.3.1 General Characteristics

Brasses are readily worked by casting, drawing, spinning and machining. They have a pleasing colour ranging from the red of copper through browner bronze-like hues and gold (jewelry brass closely resembles the colour of 14 carat gold).

The corrosion resistance of brasses (especially monophasic alpha brasses) is generally good, given that their behaviour is similar to that of copper. However, there are two particular corrosion phenomena, typical of brass, called dezincification and seasoning cracks.

The two most widely used compositions are 70-30 brass and 60-40 brass. Their compositions are shown in the phase diagram in Figure 2.3.

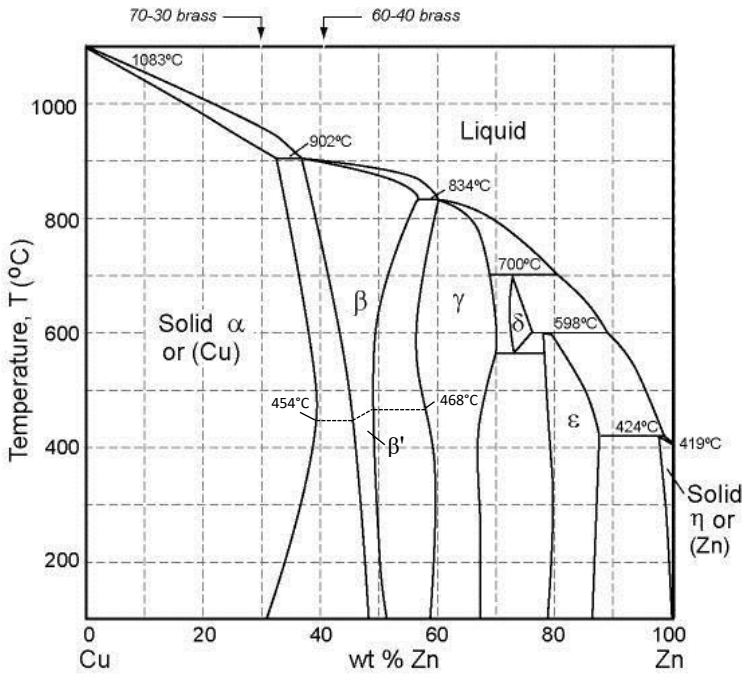

Figure 2.3 *Cu-Zn phase diagram.*

The system consists of a series of solid solutions, on which the following observations can be made: the solubility of zinc in copper gives rise to a solid solution α and increases as the T drops from 902°C to 454°C.

These brasses, whose composition falls in the alpha solid solution range, have an FCC structure: they are therefore very plastic and cold-deformable alloys by rolling, drawing and deep-drawing, and more difficult to work in hot conditions.

Between 454°C and 468°C, the β disordered solid solution (BCC) presents a β' ordered solution lattice reordering, in which zinc occupies the center of the body-centered cubic lattice. [3] [17] [19] [20] [21]

2.3.2 Typical Uses

Alloys containing up to 10% zinc are red (*Tombak*) and are typically used for special purposes (wire mesh for sieves, artistic objects, jewellery, medals, etc.).

With zinc contents from 20% to 36% we have brasses for plastic working, yellow in colour.

The best types, used for the production of shells, wires, pipes, plates, frames, taps, etc., contain from 28% to 33% zinc.

The most used in this category is the 70-30 (or *Cartridge brass*), utilized for example for deep drawn parts such as cartridge and shell casings, musical instruments and other objects made by sheet-metal working, decorative components for architecture, marine components, condenser and cooling units, jewelry, etc.

If the zinc concentration is between 37% and 45% we have brasses for castings or for plastic processing by hot drawing.

Brass with 40% zinc is called *Muntz metal* and is particularly used for tube plates of capacitors, heat exchangers, valve and pump parts, taps and water pipes, fasteners and springs.

The appearance in these alloys of the β phase (body-centered cubic) gives opposite characteristics to those of the α phase alone: in fact, α+β brasses are easily deformable in hot conditions (by rolling, extrusion and pressing), but difficult to work in cold ones.

Brasses with a completely β structure (Zn > 45%) have very few applications due to their hardness and fragility: in fact, over 50% zinc gives rise to the γ phase, without systems that slide easily and are therefore very fragile.

Then, there are the so-called *special brasses*: copper and zinc alloys that, thanks to the addition of more or less large quantities of other elements, acquire special properties.

For example, tin greatly increases the hardness and corrosion resistance of the alloy.

Among the brass containing tin are the *admiralty brass* (P-CuZn28Sn1), so called because used for naval condenser tubes, and *naval brass* (P-CuZn38Sn1), which resists particularly corrosion in marine water.

Similar effects have the addition of aluminium, which in addition improves erosion resistance due to turbulent water.

Manganese also hardens the alloy and increases corrosion resistance in seawater, as well as inhibiting crystalline grain growth during heat treatments.

In the brass that must be machined to the tool, 1-3% of lead is added to improve the machinability, interrupting the continuity of the chip and facilitating its detachment.

It should be noted that in special brass the additional elements are not added individually, but coupled in various ways to achieve a synergistic action. [3] [17] [19] [20] [21]

Table 2.2 *Most used CuZn alloys*

Alloy	Composition [%]				Delivery state	Rm [N/mm²]	$R_{p\,(0,2\%)}$ [N/mm2]	A_5 [%]	HB 10/500/30
	Cu	**Zn**		**others**					
G-CuZn25 **G-Cu27Pb2**	75 60	25 27	Pb2 Pb2	Sn2 Sn1	Cast sand	190-220 280-370	80-110 90-120	18-40 25-40	HV 45-60 HV 60-70
P-CuZn10 **(P-OT90)**	90	10		≤0.30	R H20	≤290 370-450	≤105 325-430	44 12	75 95-130
P-CuZn20 **(P-OT70)**	80	20		≤0.30	R H20	≤330 420-480	≤115 345-400	47 18	70 110-145
P-CuZn30 **(P-OT70)**	70	30		≤0.50	R H20	≤350 425-510	≤130 360-480	55 23	70 105-160
P-Cuzn40 **(*Muntz metal*)**	60	40		≤0.50	R H20	≤430 485-610	≤305 345-590	35 5	75-100 130-180
P-CuZn28Sn1 **(*Admiralty brass*)**	72	27	Sn1		Extruded	400-520	390-420	20-10	160-190
P-CuZn38Sn1 **(N*aval brass*)**	62	37	Sn1		Rolled	≤400	≤170	≤35	≤110
CuNi18Zn20 **(*alpacca 62/18*)**	62	20	Ni18		R H	400-420 530-790	160-190 370-680	55-40 12-2	HV 80-100 HV 155-210

CHAPTER 3
Preparation of the specimens

In this research work, samples of three different materials were used: AISI 304 stainless steel, pure copper and CuZn alloys.
In particular, the latter have been tested with four different compositions: CuZn15, CuZn30, CuZn33 and CuZn37.
The initial metal plates were initially heat treated, if necessary, and then cut into the final specimens with the desired geometry.
Then these were rolled under different temperature conditions (room temperature, 100 °C and in liquid nitrogen) and varying the level of deformation.
Finally, the specimens were analysed using different techniques.

3.1 Heat treatment and Hardness test

For copper and CuZn alloys, a recrystallization heat treatment was required because their microstructure had been modified following previous cold rolling operations.
The heat treatment was carried out in a *Kaloria Hotechnikai* Kft furnace, for a time of 30 minutes at a temperature of 500°C.
In Figure 3.1 are represented the samples before and after the heat treatment in the furnace.

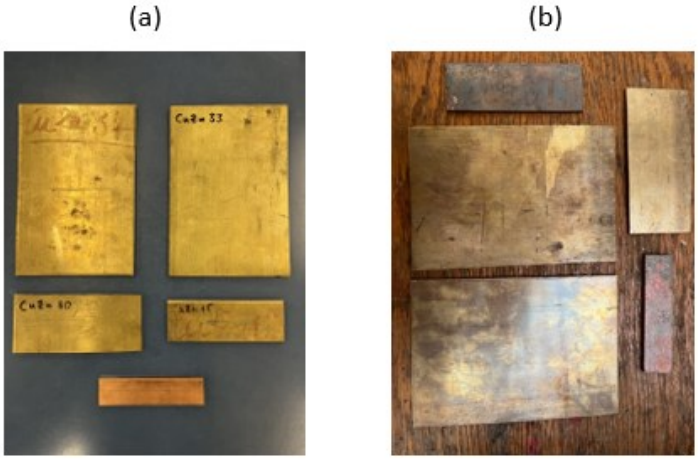

Figure 3.1 *Samples before (a) and after (b) the heat treatment.*

It's possible to notice the antioxidant effect of zinc: in fact, the alloys showed a lower amount of surface oxide than pure copper.

Subsequently a preliminary grinding was done to try to eliminate as much as possible the oxide layer from the samples.

Finally, a Brinell hardness test was made to evaluate the effectiveness of the heat treatment in the samples. The test is carried out using as a penetrator a steel sphere with diameter D having a predetermined hardness (HV ≥ 850)

The penetrator is compressed on the surface of the test piece with a pre-determined load P with an application time that varies in relation to the sample material.

It's measured the depth h (under load) or the diameter d of the indentation thus produced (after removing the penetrator) and the Brinell hardness is defined as the ratio between the load P applied [N] and the area S [mm^2] of the surface of the spherical shell that constitutes the indentation.

$$HB = 0.102 \cdot \frac{P}{S} = 0.102 \cdot \frac{p}{\pi D h} = \frac{2 \cdot 0.102P}{\pi D \cdot (D - \sqrt{D^2 - d^2})}$$

It is always good to choose, where possible, the sphere having the largest diameter in order to test the greater surface area of the material and then mediate the hardness of the structural heterogeneities possibly present.

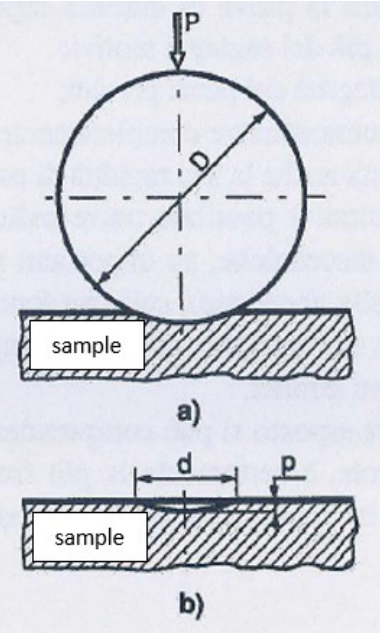

Figure 3.2 *Schematic illustration of the penetrator (a) and the indentation (b) in Brinell Hardness.*

In particular, five measurements were taken for each composition before and after recrystallization using a *Lynx Hardness Tester (l*oad applicated: 100 g, time of the loading: 5 seconds, pre-load: max).

The average values obtained are reported in Figure 3.3. [1] [3] [6]

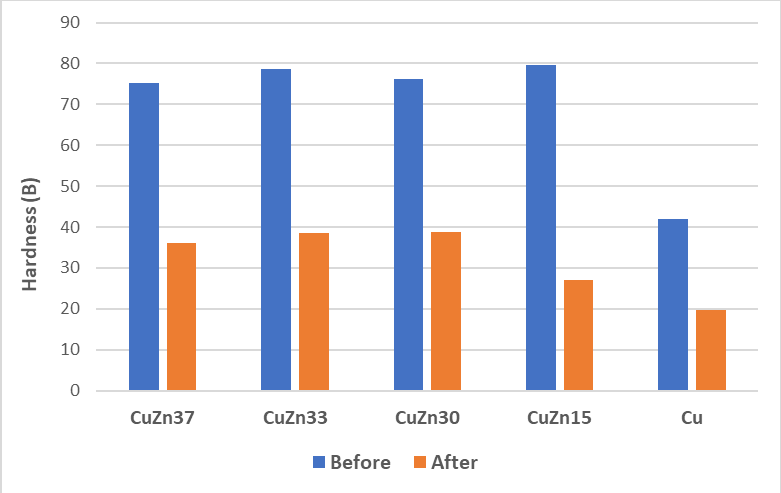

Figure 3.3 *Brinell Hardness of the samples before and after the heat treatment.*

3.2 Rolling

After the heat treatment, the samples were cut to obtain several specimens of the same composition. At this point the samples were rolled, changing the level of deformation and the temperature.

In particularly, the specimens of the same compositions were worked in three different temperature conditions: in liquid nitrogen, at room temperature and at 100°C.

For the copper and the CuZn alloys the different levels of deformation were obtained with a progressive decrease of 0.5 mm in the thickness of the specimen; instead for the stainless steel it was first verified the maximum deformation achievable before the bending became too significant (sample 5 at Room Temperature) and subsequently it was divided into equivalent steps in the remaining samples.

The deformation was evaluated in two different ways, using the variation of the thickness *w (a)* or the variation of the section *(b)* of the different specimens.

$$(a)\quad \Delta H[\%] = \frac{w_i - w_o}{w_0} \times 100$$

$$(b)\quad \Delta Area[\%] = \frac{|Area_i - Area_0|}{Area_0} \times 100$$

Except for the sample number 1, the other levels of deformation were reached using multiple steps of rolling.

3.2.1 Rolling in Liquid Nitrogen

In this case the samples were immersed in the liquid nitrogen (~77 K), causing its boiling (characterized by the presence of bubbles rising to the surface).

The rolling process began when the bubbles stopped forming, indicating that the specimens had reached the desired temperature.

The characterization of the deformations obtained are reported in Table 3.1.

Table 3.1 *Deformation levels of the samples rolled in liquid nitrogen.*

Material	Sample	w_0 [mm]	w_i [mm]	h_0 [mm]	h_i [mm]	$Area_0$ [mm^2]	$Area_i$ [mm^2]	ΔH [%]	Δarea [%]
AISI 304	**1**	13,5	13,6	5,1	4,8	68,85	65,28	**5,88**	**5,19**
	2	12,2	12,4	5,1	4,5	62,22	55,80	**11,76**	**10,32**
	3	13,9	14,2	5,1	4,2	70,89	59,64	**17,65**	**15,87**
	4	15,1	15,6	5,1	3,7	77,01	57,72	**27,45**	**25,05**
Cu	**1**	12,5	12,7	5,9	5,5	73,75	69,85	**6,78**	**5,29**
	2	11,7	12	5,7	4,8	66,69	57,60	**15,79**	**13,63**
	3	10,6	11	5,9	4,3	62,54	47,30	**27,12**	**24,37**
	4	11,7	12,4	5,9	3,8	69,03	47,12	**35,59**	**31,74**
	5	12,1	12,7	5,9	3,4	71,39	43,18	**42,37**	**39,52**
CuZn15	**1**	11,8	12	5,4	4,9	63,72	58,80	**9,26**	**7,72**
	2	10,6	10,9	5,4	4,5	57,24	49,05	**16,67**	**14,31**
	3	11,7	12	5,4	3,8	63,18	45,60	**29,63**	**27,83**
	4	10,6	11,3	5,4	3,3	57,24	37,29	**38,89**	**34,85**
	5	11,8	12,6	5,4	2,7	63,72	34,02	**50,00**	**46,61**
CuZn30	**1**	12	12,4	4,5	3,8	54,00	47,12	**15,56**	**12,74**
	2	12	12,6	4,5	3,5	54,00	44,10	**22,22**	**18,33**
	3	12,1	12,8	4,5	2,9	54,45	37,12	**35,56**	**31,83**
	4	12,1	12,9	4,5	2,5	54,45	32,25	**44,44**	**40,77**
	5	12	13,1	4,5	2	54,00	26,20	**55,56**	**51,48**

Material	Sample	w_0 [mm]	w_i [mm]	h_0 [mm]	h_i [mm]	$Area_0$ [mm^2]	$Area_i$ [mm^2]	ΔH [%]	Δarea [%]
CuZn33	**1**	12,1	12,3	4,7	4,2	56,87	51,66	**10,64**	**9,16**
	2	12	12,5	4,8	3,8	57,60	47,50	**20,83**	**17,53**
	3	12,2	12,7	4,8	3,3	58,56	41,91	**31,25**	**28,43**
	4	12	12,8	4,8	2,7	57,60	34,56	**43,75**	**40,00**
	5	12	13	4,9	2,2	58,80	28,60	**55,10**	**51,36**
CuZn37	**1**	12	12,3	4,7	4,2	56,40	51,66	**10,64**	**8,40**
	2	12,1	12,5	4,6	3,7	55,66	46,25	**19,57**	**16,91**
	3	12,2	12,7	4,6	3,2	56,12	40,64	**30,43**	**27,58**
	4	12,2	12,8	4,6	2,6	56,12	33,28	**43,48**	**40,70**
	5	12,2	12,9	4,6	2,1	56,12	27,09	**54,35**	**51,73**

3.2.2 Rolling at Room Temperature

At this condition the samples were simply rolled after the cutting operations.

The number 0 indicates the reference samples (not rolled).

The deformation levels obtained are shown in Table 3.2.

Table 3.2 *Deformation levels of the samples rolled at room temperature.*

Material	Sample	w_0 [mm]	w_i [mm]	h_0 [mm]	h_i [mm]	$Area_0$ [mm^2]	$Area_i$ [mm^2]	ΔH [%]	Δarea [%]
AISI 304	**0**	13,8	-	5,2	-	71,76	-	**-**	**-**
	1	14,8	15	5,1	4,8	75,48	72,00	**5,88**	**4,61**
	2	15	15,2	5,2	4,6	78,00	69,92	**11,54**	**10,36**
	3	13,7	13,9	5,2	4,3	71,24	59,77	**17,31**	**16,10**
	4	12,8	13,3	5,2	3,8	66,56	50,54	**26,92**	**24,07**
	5	14,1	14,9	5,2	3,6	73,32	53,64	**30,77**	**26,84**
Cu	**1**	12,1	12,2	6,6	6,1	79,86	74,42	**7,58**	**6,81**
	2	12,2	12,6	6,9	5,8	84,18	73,08	**15,94**	**13,19**
	3	12,4	13	6,6	5	81,84	65,00	**24,24**	**20,58**
	4	11,6	12,3	6,6	4,6	76,56	56,58	**30,30**	**26,10**
	5	12,4	12,9	6,9	4,4	85,56	56,76	**36,23**	**33,66**
	6	12,2	13,1	6,8	3,8	82,96	49,78	**44,12**	**40,00**

Material	Sample	w_0 [mm]	w_i [mm]	h_0 [mm]	h_i [mm]	$Area_0$ [mm^2]	$Area_i$ [mm^2]	ΔH [%]	Δarea [%]
CuZn15	**0**	11,4	-	5,3	-	60,42	-	**-**	**-**
	1	11,3	11,5	5,3	4,7	59,89	54,05	**11,32**	**9,75**
	2	11,1	11,4	5,4	4,5	59,94	51,30	**16,67**	**14,41**
	3	11,9	12,4	5,3	3,8	63,07	47,12	**28,30**	**25,29**
	4	11,6	12,1	5,9	3,8	68,44	45,98	**35,59**	**32,82**
	5	11,3	11,8	5,3	2,8	59,89	33,04	**47,17**	**44,83**
	6	10,8	11,8	5,3	2,3	57,24	27,14	**56,60**	**52,59**
CuZn30	**0**	12	-	4,4	-	52,80	-	**-**	**-**
	1	11,9	12	4,4	3,8	52,36	45,60	**13,64**	**12,91**
	2	11,9	12,4	4,5	3,5	53,55	43,40	**22,22**	**18,95**
	3	12	12,5	4,4	3	52,80	37,50	**31,82**	**28,98**
	4	11,9	12,6	4,4	2,6	52,36	32,76	**40,91**	**37,43**
	5	11,9	12,7	4,6	2	54,74	25,40	**56,52**	**53,60**
CuZn33	**0**	12	-	4,7	-	56,40	-	**-**	**-**
	1	12,1	12,2	4,7	4,2	56,87	51,24	**10,64**	**9,90**
	2	12,1	12,5	4,6	3,6	55,66	45,00	**21,74**	**19,15**
	3	12,1	12,6	4,7	3,2	56,87	40,32	**31,91**	**29,10**
	4	12	12,7	4,7	2,7	56,40	34,29	**42,55**	**39,20**
	5	12	12,8	4,7	2,2	56,40	28,16	**53,19**	**50,07**
CuZn37	**0**	11,8	-	4,7	-	55,46	-	**-**	**-**
	1	11,9	12,1	4,7	4,2	55,93	50,82	**10,64**	**9,14**
	2	12,2	12,5	4,7	3,8	57,34	47,50	**19,15**	**17,16**
	3	12,1	12,7	4,7	3,2	56,87	40,64	**31,91**	**28,54**
	4	12,2	13,1	4,9	2,9	59,78	37,99	**40,82**	**36,45**
	5	12	13	4,6	2,1	55,20	27,30	**54,35**	**50,54**

3.2.3 Rolling at 100°C

The boiling water was used to obtain this temperature condition.

Specifically, a cooker was used to heat the water and, once the bubbles began to form, the samples were kept inside for 5 minutes before starting the rolling process.

The deformations of the different compositions are reported in Table 3.3.

Table 3.3 *Deformation levels of samples rolled at 100°C.*

Material	Sample	w_0 [mm]	w_i [mm]	h_0 [mm]	h_i [mm]	$Area_0$ [mm^2]	$Area_i$ [mm^2]	ΔH [%]	Δarea [%]
AISI 304	**1**	13,5	13,7	5,1	4,8	68,85	65,76	**5,88**	**4,49**
	2	12,9	13,2	5,1	4,5	65,79	59,40	**11,76**	**9,71**
	3	16,7	17,1	5,1	4,2	85,17	71,82	**17,65**	**15,67**
	4	13,8	14,3	5,1	3,6	70,38	51,48	**29,41**	**26,85**
Cu	**1**	11	11,2	5,9	5,4	64,90	60,48	**8,47**	**6,81**
	2	11,9	12,2	5,9	4,9	70,21	59,78	**16,95**	**14,86**
	3	11,8	12,4	5,9	4,3	69,62	53,32	**27,12**	**23,41**
	4	11,6	12,5	5,9	3,8	68,44	47,50	**35,59**	**30,60**
CuZn15	**1**	12	12,1	5,5	5,1	66,00	61,71	**7,27**	**6,50**
	2	10,6	10,8	5,5	4,5	58,30	48,60	**18,18**	**16,64**
	3	11,9	12,3	5,5	4	65,45	49,20	**27,27**	**24,83**
	4	11,4	12	5,4	3,5	61,56	42,00	**35,19**	**31,77**
	5	11,2	12,1	5,4	2,9	60,48	35,09	**46,30**	**41,98**
CuZn30	**1**	12,1	12,3	4,5	4	54,45	49,20	**11,11**	**9,64**
	2	11,9	12,3	4,5	3,5	53,55	43,05	**22,22**	**19,61**
	3	12	12,6	4,5	2,9	54,00	36,54	**35,56**	**32,33**
	4	12	12,8	4,5	2,4	54,00	30,72	**46,67**	**43,11**
	5	12	13	4,5	1,8	54,00	23,40	**60,00**	**56,67**
CuZn33	**1**	12	12,2	4,9	4,3	58,80	52,46	**12,24**	**10,78**
	2	12,1	12,5	4,8	3,8	58,08	47,50	**20,83**	**18,22**
	3	12	12,5	4,7	3,2	56,40	40,00	**31,91**	**29,08**
	4	12,1	12,7	4,8	2,7	58,08	34,29	**43,75**	**40,96**
	5	12	12,8	4,8	2,3	57,60	29,44	**52,08**	**48,89**
CuZn37	**1**	12,2	12,3	4,6	4	56,12	49,20	**13,04**	**12,33**
	2	12,1	12,4	4,6	3,7	55,66	45,88	**19,57**	**17,57**
	3	12,1	12,5	4,6	3,2	55,66	40,00	**30,43**	**28,14**
	4	12	12,6	4,7	2,7	56,40	34,02	**42,55**	**39,68**
	5	12,1	13	4,6	2,1	55,66	27,30	**54,35**	**50,95**

3.3 Grinding and Polishing

To obtain a surface suitable for the following analysis, the rolled samples were subjected to grinding and polishing operations.

In particular, in the samples of pure copper and CuZn alloys, because their small size, it was preferred to resort to a resin mounting to facilitate the treatment; in this way the samples with different deformation of the same composition have been collected in a single resin specimen.
This operation was carried out using rubber supports, filled with powder of the acrylic resin and hardening liquid (both *Duracryl® Plus*); the chemical reaction hardening phase took place inside a pressure device in about 15/20 minutes.
The final result is shown in Figure

Figure 3.4 *Samples of copper and CuZn alloys mounted in resin.*

For the grinding operations, SiC abrasive papers with increasing grit number (and consequently decreasing particles size) were used.
The sequenc usede was P180 (equal to a diameter of the abrasive particles of 90-75 μm), P320 (46 μm), P600 (26 μm), P1200 (15 μm), P2500 (12 μm) and finally P400 (6 μm).
Instead, for the polishing operations the samples were worked with cloth sprinkled with abrasive aqueous solutions based on diamond paste (3 μm and then 1 μm).
These operations have to be carry out carefully, must not harden or overheat the material.

CHAPTER 4
OM analysis of Copper and CuZn alloys

Optical Microscope technique is the common first step for metallographic analysis of metallic materials because it allows to examine the material structure.

It also allows to see which phases are present, their quantity, their size and their distribution. Therefore, Optical Microscope technique is the first step to be taken in order to learn which material we are working with.

This technique allows to have a previously knowledge about the presence of materials defects such as porosity, non-metallic inclusions or cracks, and it is also very useful in order to evaluate the effect that external processes such as heat, thermo-chemical and thermomechanical treatments, hot and cold plastic deformation that could be on the material.

This instrument uses the light reflected by the metal surface that appears different in color and intensity as a result of the different corrosion made by chemical reagents in various areas.

More specifically, the surface to be observed is resting on a table, adjustable through two micrometric screws, at the center of which there is a hole for the passage of light.

The light from a source, opportunely collimated by diaphragms and capacitors, is directed through a mirror to the surface of the specimen after passing through the lens.

The reflected light is concentrated again in the objective; the light signal is diverted from the prism towards the eyepiece lens that allows the enlarged vision of the sample.

The signal can then be diverted from a mirror and sent to a photo screen or camera.

The simplified scheme of the optical microscope is represented in Figure.

The analysis was done at the BME University of Budapest with *Olympus PMG3*, using the software *Olympus DPcontroller* for the image acquisition.

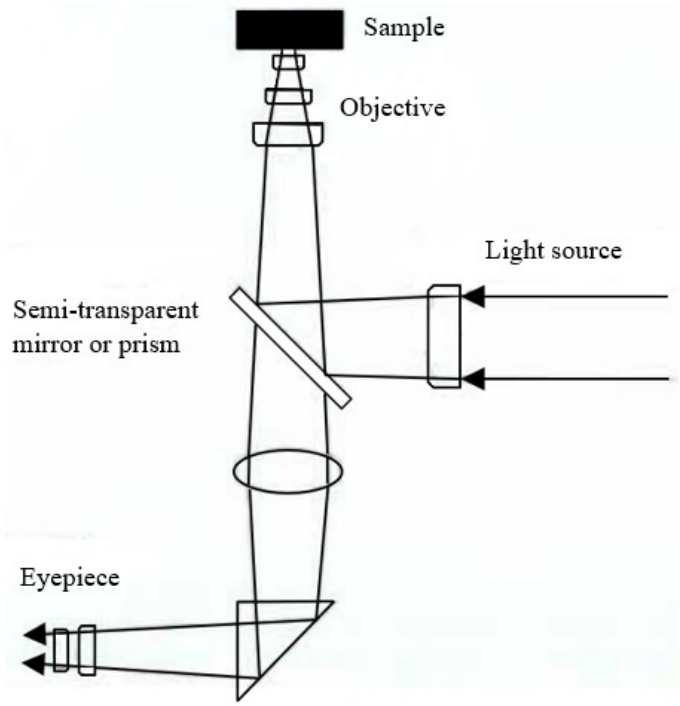

Figure 4.1 *Schematic illustration of the optical microscope.*

4.1 Etching

Chemical etching was carried out on copper and CuZn alloys to highlight the crystalline structure in the subsequent optical microscopy analysis.

In general, the chemical composition of the reagents depends on the nature of the metal alloy or the phases to be highlighted and allows selective corrosion on the surface areas with higher energy. The chemical etching has a double function: oxidizing against areas with a higher energy content and leaching for the oxidation products to detach them from the surface.

Specifically, in this case *Rez* has been used as an etching agent, consisting of 100 mL of distilled water, 25 mL of HCl and 5 g of iron chloride.

Each sample was first washed with water, sprayed with ethanol and then dried to remove any residue from previous grinding and polishing steps.

Then it was treated with a cotton swab soaked in the etching agent, washed again with water, sprayed with ethanol and finally dried.

The use of ethanol allows to avoid the formation of stains by evaporating the water, thus allowing to obtain better images with the microscope.

In many cases a single etching step was not enough and therefore the treatment was carried out several times to obtain an adequate surface.
In the figure you can see the difference in the images obtained under the optical microscope after only one etching and after two etching steps.

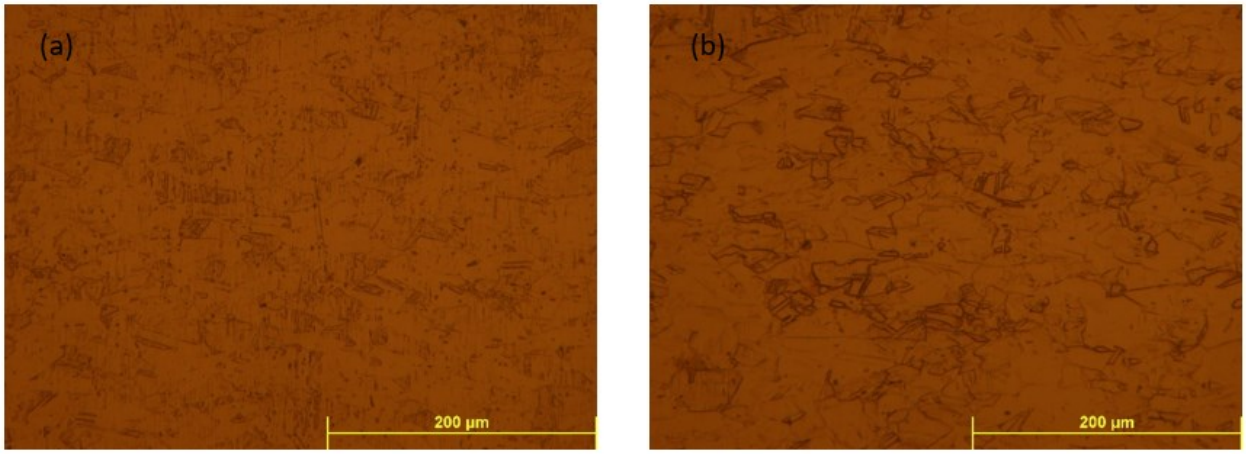

Figure 4.2 *Micrography of CuZn30 rolled at 100°C (200x) after (a) single step and (b) two steps of etching.*

4.2 Detection of the twin boundaries

Through the images obtained from the optical microscope it was possible to evaluate the effect of the composition, deformation and temperature in terms of twinnings present.
To quantify their presence, it was decided to use to a sort of density ϕ defined as:

$$\phi = \frac{\sum_{i=0}^{n} l_i}{A} \quad [\mu m^{-1}]$$

Where l_i [µm] represents the length of the single twin boundary and A [μm^2] is equal to the area of the micrography.
The data used in the equation were calculated using the software *ImageJ*.
An example is shown in Figure 4.3.

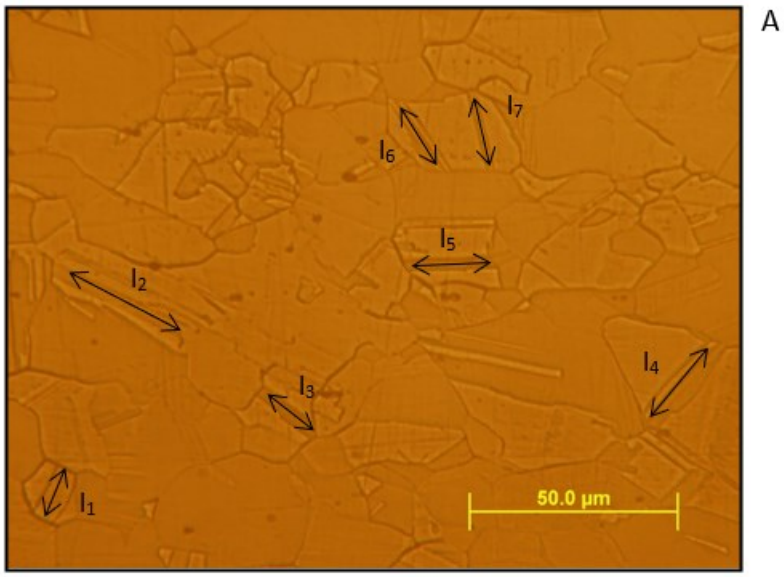

Figure 4.3 *Example of the detection of the twin boundaries with a length equal to* l_i

For each sample, the density of the twin boundaries was calculated at three different points in the specimen with a magnification of 500x and the average value was subsequently reported.

CHAPTER 5
Experimental analysis on AISI 304 steel

To evaluate the effect of the different deformations in the three temperatures on AISI 304 steel, hardness analyses and magnetic investigations were performed on the samples, which include measurements of ferrite content, Barkenhause noise and coercivity.
All measurements were carried out at the BME University of Budapest.

5.1 Vickers Hardness Test

The hardness test allows to measure the strength of a material, specifically its resistance to penetration by a harder body, which moves slowly in perpendicular direction to the specimen's surface with a certain load.
In practice, on the surface of the material to be tested is compressed this body, called penetrator, which has well defined shape and dimensions: the whole process is carried out in standardized mode defined by the various unification entities.
Hardness tests are carried out to obtain a conventional index from which direct or indirect information can be derived about the quality and properties of the material, its composition, its state, the nature and mechanical characteristics of the surface, in addition to the variation of structural constituents.
The Vickers hardness test specifically uses a penetrator consisting of a square-based diamond pyramid with an angle at the vertex of 136°.
The use of the diamond penetrator provides with the same load a continuous scale of hardness, suitable for both annealed and hard metal materials: this results from the strict dependence of the test on the applied load, as the footprints are always geometrically similar.
The hardness is determined by the following relationship:

$$HV = 0.102 \cdot \frac{P}{S} = \frac{2 \cdot 0.102 \cdot P \cdot sin\left(\frac{136°}{2}\right)}{d^2} = 0.1891 \cdot \frac{P}{d^2}$$

where P is the applicated load [N], S is the lateral surface area of the indentation [mm^2] and d is the average of the pyramidal footprint diagonals d_1 and d_2 detected after loading [mm].

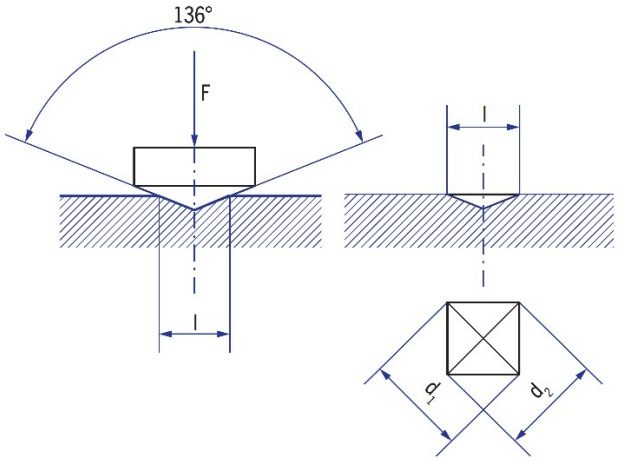

Figure 5.1 *Schematic illustration of the penetrator and indentation in Vickers Hardness.*

Vickers hardness is related to the breaking stress of the material by the relationship:

$HV = 0.3 \cdot R_m$

The normal test load for steel required by UNI standards is 294 N (= 30kg), instead the time of application of the full load is usually from 10 to 15 seconds.

The distance of the centre of a footprint from the edges of the workpiece or the contour of another footprint shall not be less than 2.5d.

In addition, no deformation shall be visible on the face opposite the test face.

Given the small size of the footprint, the state of the surface takes on significant importance: the roughness can in fact mask or alter the footprint and it's therefore advisable to carry out a delicate metallographic cleaning of the surface.

As shown in Figure 5.2, sometimes the indentation deviates from the perfectly square shape *(a)*, mainly influenced by the hardening coefficient m.

It is evident that these two conditions (typical respectively of soft or annealed materials and hard or hardened materials) alter the measurement of the footprint surface, so that in the first case *(b)* a value of the footprint area greater than the real one and therefore a value of the Vickers hardness lower, and vice versa in the second case *(c)*.

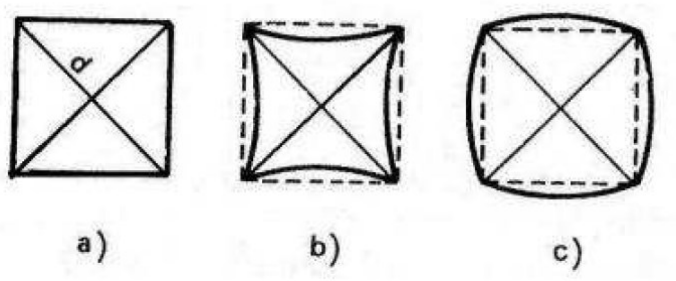

Figure 5.2 *Examples of indentation shapes.*

This testing methodology represents the great advantage of using the same type of indenter for all types of material without having to change the test scale as happens for the Brinell or Rockwell test.

Despite this, the Vickers hardness is not very widespread except in the scientific field or in the case of very hard materials; in fact, the test is relatively long, requires special machines, requires careful preparation of the test and reading the diagonals.

It is also not suitable for measuring the hardness of materials with a highly heterogeneous structure, such as grey cast iron.

KB Pruftechnik Hardness Tester was used for the experimental measurements, working with a load of 30 Kg and an application time of 12 seconds. [1] [3] [6]

5.2 Magnetic Investigations

Regarding stainless steel, magnetic tests are a valid instrument for analysis. They can be used to find any kind of variation of ferromagnetic phase content in the material.

Phases in the same material can have a different behaviour. It is the case of austenitic and ferritic phase that are respectively paramagnetic and ferromagnetic and ε-martensite and α'-martensite that are respectively paramagnetic and ferromagnetic. Thanks to their behaviour it is possible to carry out several magnetic tests.

5.2.1 Fundamentals of Magnetism

Magnetism is the phenomena by which some materials demonstrate an attractive or repulsive force or influence on other materials, thanks to the movements of electric charges which originate a

magnetic field. The majority of materials doesn't show particular behaviour under the effect of a magnetic field, instead some of them, under its application, manifest different effects such as attraction, repulsion or magnetization.

To describe the magnetism, it's necessary to introduce some quantities: H is conventionally defined as the magnetic field applied and B is the field generated into the material after the application of H.

They are related by the following equation:

$$B = \mu_0(H + M)$$

where μ_0 is the vacuum permeability and M is the magnetization, which expresses the contribution of the material at the field generated and allows to describe directly the magnetic properties of the material.

H is expressed in $[A \cdot m]$, B in $[T]$, M in $[A \cdot m]$ and μ_0 in $[H \cdot m]$ or equivalently in $[N \cdot A^2]$.

Other important quantities to characterize the magnetic properties of the material are the relative magnetic permeability μ_r and the susceptibility χ_m (which gives an idea of how much the material is influenced by the magnetic field), which are related by:

$$\chi_m = \mu_r - 1$$

The macroscopic magnetic properties of materials are consequence of the magnetic moments associated with individual electrons.

The total magnetic moment of an atom is due to two sources: the first is the orbital motion of the electron around the nucleus (assimilated to close circuit current) and gives the orbital magnetic moment; the second is due to the fact that each electron has its own spin and related to this there is an intrinsic magnetic moment.

The two contributions are shown in Figure 5.3.

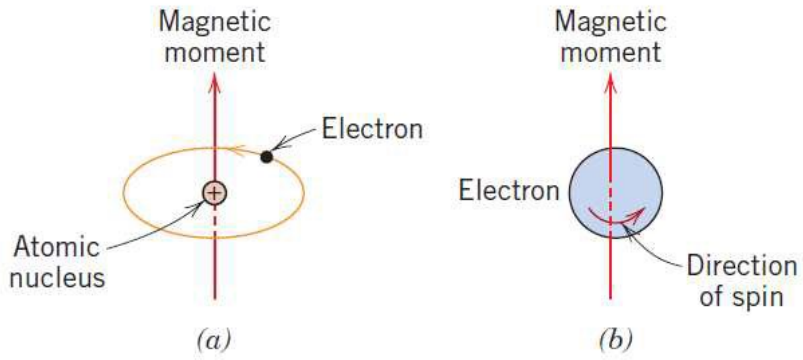

Figure 5.3 *Contributions of the total magnetic moment: orbital(a) and intrinsic (b) magnetic moments.*

However, each atom or molecule of the material acquires, under the application of an external magnetic field, an average magnetic moment <m> oriented parallel to the field B. Taking this average <m>, considering Δt a little volume of material and ΔN the number of atoms into this volume, it's possible to write the magnetization M as:

$$M = \left(\frac{\Delta N}{\Delta t}\right) * < m >$$

But M can be expressed also in this other way:

$$M = \chi_m \cdot H$$

So, from this it's clear that χ_m can give some information of how much a material magnetizes itself under a magnetic field. Specifically, χ_m can vary from 10^{-5} A/m (soft magnetic material) to 10^{6} A/m (hard magnetic material).

Combining the equations found it's possible to write:

$$B = \mu_0(H + M) = \mu_0(H + \chi H) = \mu_0(1 + \chi)H = \mu_0\mu_r H = \mu H$$

From which it's possible to define the relative permeability μ_r of the material as:

$$\mu_r = 1 + \chi$$

[2] [7] [8] [9] [16]

5.2.2 Classification of Magnetic Materials

All materials can be divided, considering their magnetic behaviour, into five categories: diamagnetism, paramagnetism, ferromagnetism, ferrimagnetism and antiferromagnetism. The two more common types of magnetic materials are the first two groups and they are generally defined

as non-magnetic materials because their interactions between individual moments aren't enough strong to generate a domain structure, while the materials of the other groups are those that are known as magnetic materials in which it's possible to detect a very strong interaction between neighbouring moments that causes a self-organize process called spontaneous magnetization (which results in a domain structure).

- *Diamagnetic materials*

In the diamagnetic substances the μ_r is constant with the variation of B and < 1 and this means small and negative values of the susceptibility ($\chi_m = -10^{-5} \div -10^{-7}$).

In this case the amperian currents (currents of atomic origin formed by the effect of the magnetic field produced by the conduction current) give an opposite contribution to the applied magnetic fields and so, also with a very strong field, the magnetization generated (opposite to the field) is very weak.

Consequently, diamagnetism is a very weak form of magnetism that happens in materials which have structural atoms with two free electrons at the same energy but opposite spin (therefore magnetic moments are compensated each other). In this case, when an external field is applied, it generates a torque that changes the orbital motion of the electrons, developing a magnetic moment that has opposite direction to the external field. This phenomenon is not permanent, and it persists only as long as an external field is being applied. If the external field is turned off, the initial situation of zero net magnetic moment is recovered.

Some examples of this kind of materials are copper, silver and gold.

- *Paramagnetic materials*

In these substances there is an asymmetry condition where there is not compensation of the magnetic moments (due to presence of unpaired electrons that, due to their spin, can behave like magnetic dipoles), therefore each atom have an intrinsic magnetic moment but in absence of external magnetic field the orientation of these moments is random, so the magnetization results macroscopically zero.

Instead, when an external magnetic field H is applied, there is a partial orientation of the moments that gives a magnetic moment <m> aligned and proportional to the field applied.

In this case, magnetization and external applied magnetic field are concordant but, as for the diamagnetic, turning off the external field the total magnetization moment returns to zero.

They show relative permeabilities μ_r constant with the variation of B and > 1, with small and positive values of the susceptibility ($\chi_m = 10^{-3} \div 10^{-5}$).

Some examples are aluminium, platinum and manganese.

- *Antiferromagnetic materials*

In these substances, the magnetic moments of atoms or molecules are aligned in a regular pattern with neighbouring spins (on different sublattices), but with opposite directions. When two magnetic moments are close enough to have sufficient overlap of their wavefunctions, there is a strong but short-range coupling which decreases rapidly as the ions are separated. Considering as example two atoms with one electron each: when these atoms are very close together, the Coulomb interaction is minimal when the electrons spend most of their time in between the nuclei. Since the electrons required to be at the same place at the same time, the exclusion principle of Pauli requires that they possess opposite spins. This gives rise to anti-parallel alignment.

An example of these kind of materials is chromium.

- *Ferrimagnetic materials*

As in antiferromagnetic, these substances have the magnetic moments of the atoms on different sublattices opposed, but the opposing moments are not equal and a spontaneous magnetization remains. This happens when the sublattices consist of different materials or ions (such as Fe2+ and Fe3+).

As antiferromagnetic materials, also in ferrimagnetism there is a conservation of the magnetization when the applied field returns to zero.

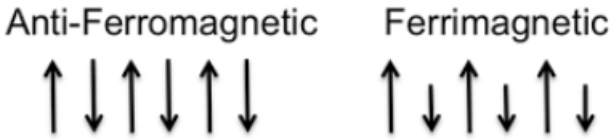

Figure 5.4 *Representation of the magnetic moments in antiferromagnetic and ferrimagnetic materials.*

- *Ferromagnetic materials*

Ferromagnetic substances are the most widely recognized due to their very large permanent magnetization. For these materials the susceptibility is positive and can reach very high values, typically about χ_m = 50 to 10˙000, while the relative permeability is usually $\mu_r = 10^3$-10^4.

These materials have a permanent magnetic moment mainly given by unpaired electron spin, and with little contribution by orbital magnetic moment. Even without external field, the coupling interactions cause net spin magnetic moments of closest atoms to align to one another. According with this positive interaction between magnetic moments, there are many small regions called domains (or Weiss domains) in which the direction of the magnetic moments is the same. In this case, the magnitude of the magnetization field for the whole solid is given by the vector sum of the magnetization of all domains.

When an external magnetic field is applied, the walls of these domains, that divide a domain from another one, start to move and the modification of the domain size begins. In this process, shown in Figure 5.5, there is an increasing in size of those domains that show a parallel magnetization to H and a decreasing in size of those domains that are not parallel. The material will saturate when all the domains will be aligned and it normally happens by increasing the external field. The saturation magnetization is the maximum magnetization that can be obtained with a magnetic field.

In any case, once the external field H is turned off, a residual magnetization will remain inside of the material. This behaviour is also caused in this case by the presence of defects such as dislocations that avoid reversible movements of walls.

If the material is demagnetized, the appropriately weighted vector sum of the magnetization of all domains will be zero.

Examples of this class of materials are iron, cobalt, nickel and several rare earth metals and their alloys. [2] [7] [8] [9] [16]

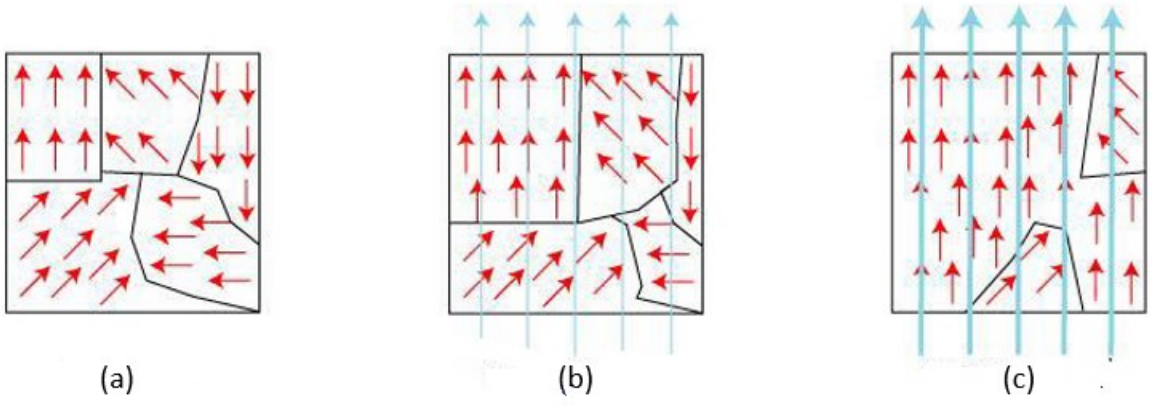

Figure 5.5 *Magnetic domains in conditions of (a) no external field, (b) small field applied and (c) strong field applied.*

5.2.3 Ferromagnetic Materials and Hysteresis Loop

The properties of the ferromagnetic substances are very different from the others and for this reason ferromagnetism is the most interesting behaviour to study.

Unfortunately for the ferromagnetic materials there is not a classical explanation of the phenomena, but it is necessary a quantum explanation which lead to say that there is a particular condition in each atom where its intrinsic magnetic moment is mainly due to the electron spin.

As a consequence, in this kind of materials, also with H=0 it's possible to obtain a magnetic moment M that can be greater than the previous H applied.

As said before, according with these positive interactions between magnetic moments, there are many small regions in a crystal of ferromagnetic material called Weiss Domains, containing more than 10^8 atoms that have some magnetic moment, and consequently magnetization, direction (due to magnetic moment interaction that align the spins). Each domain is separated from neighbouring domains by domain boundaries or walls (called *Bloch walls*), across which the direction of magnetization gradually changes. Even if each domain is magnetized the total material can have M=0 because the domains are random oriented.

When an external magnetic field H is applied, the block walls start to move, modifying the domain size, favouring the growth of those domains that have parallel magnetization to H and consequently with a decreasing of the domains where the M is not parallel.

This movement is reversible, but for higher fields the walls start a non reversible motion in which the magnetic moments of the domains start to rotate to align to the external field direction, until all the domains are oriented and the material reaches the saturation.

The motion of the walls is not reversible due to imperfections and defects (such as dislocations) so, turning off the external field H will remain a residual magnetization. Indeed, more the dislocation density, greater the impedance to domain wall motion.

Summarizing, ferromagnetic substances allow very high magnetization also if the applied field is low, with magnetic properties that can change with the composition, thermal treatment, deformations and mechanical stresses. So, it's possible to conclude that the atomic phenomena which drive the ferromagnetism derive from the crystalline structure and his modification due to thermal or mechanical operation.

Furthermore, on the contrary of paramagnetic and diamagnetic behaviour, for a ferromagnetic material there isn't a linear relation between B and H.

For this substances susceptibility and relative permeability depend from the H value and also from its way of increasing. In particular μr is not constant, so in order to characterize the properties of a given ferromagnetic material is necessary to measure the magnetization induction B as a function of H over a continuous range of H to obtain a *hysteresis curve*, represented in Figure 5.6.

The application of an external field H causes the magnetization induction B to rise, from 0 to a maximum value called *magnetization saturation* (correspondent to H_m) which remains constant also with a further increase of H. The saturation magnetization depends only on the magnitude of the atomic magnetic moment *m* and its number *n,* giving $M_{sat}=m*n$.

This is described by the *first magnetization curve (a)* and the process is possible thanks to the motion and growth of magnetic domains.

After H_m the B field arise again but of a very little rate, indeed relative permeability is very little.

Now it's possible to decrease H until 0, seeing that the values of B and M create a new different curve *(b)*, which stays above the first magnetization curve and intercepts the Y axis in a point called M_r, the *residual magnetization*.

Here the material is still characterized by some magnetization due to the magnetic domains where the field is still oriented in the direction of the previous field.

In this condition the material can be considered as a permanent magnet, because it's magnetized also without external field applied.

To reduce the induction to zero the applied filed must be reduced until H_c, the *coercive field* or *coercivity* (where M=0 and B=0), which corresponds to the strength of the magnetic field required to reduce the magnetization (or the so-called *Remanence* B_r, if H is considered in function of B) to zero.

Continuing to decrease H the situation is specular to the positive values, until the curve reaches the value $-H_m$ where the magnetization stops to decrease and remain almost constant, indicating that the material has reached again the magnetization saturation but with opposite direction.

Finally, if the H values increases again until +Hm the magnetization follow the *(c)* curve, until the rejoining with curve *(a).*

The complete closed curve is called *hysteresis loop* and can be given in terms of M or B.

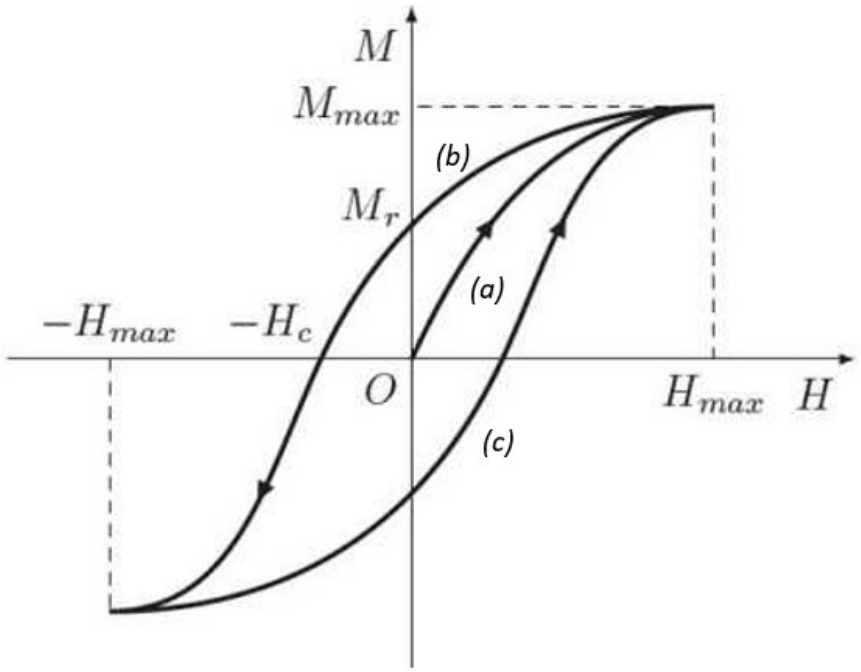

Figure 5.6 *Hysteresis loop of a ferromagnetic material.*

If H varies in the range -Hm, Hm or greater, the same loop is always obtained, while if the range of variability is reduced, narrower loops are obtained, with vertices on the curve of first magnetization.

A given value of H may correspond to infinite values of B (and therefore of μ_m and χ_m) between the curves *(b)* and *(c)*; consequently, the magnetization of a ferromagnetic substance depends, in addition to the value of H, also on its history.

In addition, the hysteresis loop represents the state diagram of the material and its shape strongly depends on the composition of the substance: it's possible to distinguish the so-called *hard materials*, whose hysteresis loop is quite wide (M_r and H_c large) or the *soft materials*, characterized by a very narrow loop (small H_c).

The formers are suitable for the construction of permanent magnets, as they have high values of M_r (almost equal to M_{sat}) and are difficult to demagnetize (high Hc); the latters are suitable for the construction of electromagnets because they are easy to magnetize and demagnetize.

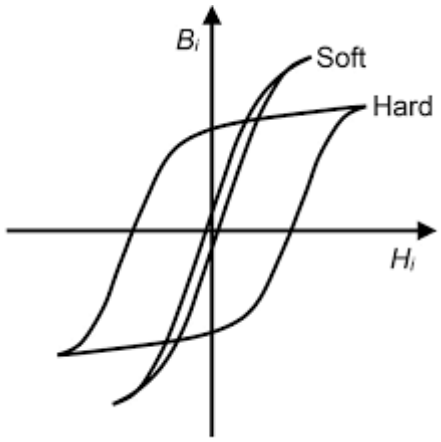

Figure 5.7 *Difference in the hysteresis loop in hard and soft materials.*

Another fundamental property of ferromagnetic materials is that for each of them there is a critical temperature Tc, known as *Curie Temperature*, above which the material becomes paramagnetic. The susceptibility is given in this case by the *second law of Curie*:

$$\chi_m = \frac{C\rho}{T - T_c}$$

Where ρ is the density of the substance and C is known as *Curie's constant*.

It is possible to extrapolate several information from the hysteresis loop; regarding the saturation magnetization, it is proportional to the ferromagnetic phase. Therefore, an increase in the value of saturation magnetization corresponds to an increase of ferromagnetic phase. [2] [7] [8] [9] [10] [16] [26]

5.2.4 Ferrite Tester

For these measurements the *Feritscope FMP30* by *Fischer*® has been used.

The ferrite tester is an instrument used all around the world, as the name says, is an instrument for the measure of the ferrite content in the steel under investigation.

The ferritescope measure according to the magnetic induction method, in which the ferrite content is determined in a quick and non-destructive way in accordance with the Basler standard and DIN EN ISO 17655.

The probe for measuring the ferrite content consists of an iron core around which an exciter coil is wound. A low frequency (168 Hz) alternating current flows through the coil. This creates an alternating magnetic field around the poles of the iron core.

When one of the probe's poles approaches a steel component, such as an iron component, the ferrite grains in the steel reinforce the alternating magnetic field. A measuring coil records this increase as voltage. The magnitude of the voltage difference depends on the magnetizable component in the crystal structure. For this reason, this method cannot distinguish between delta ferrite and strain induced martensite.

The magnetic field of the coil extends about 2-3 mm uniformly around the probe pole, both at the sides and in depth. This means that a roughly cone-shaped sample section is taken into account.

Moreover, it can also happen that the results of the magnetic-inductive method deviate significantly from the metallographic determination, because this method only records the surface distribution of ferrite.

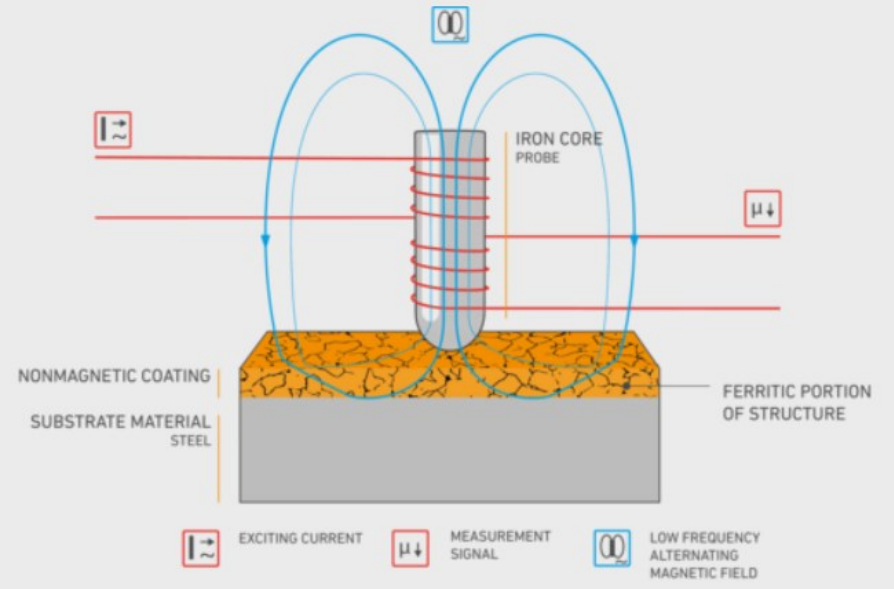

Figure 5.8 *Schematic illustration of the ferrite tester.*

Factors that mainly influence the results of a measurement include:

- Magnetic permeability

  It indicates the material's ability to adapt to a magnetic field. Substances such as iron or nickel have a high permeability. They magnetize and strengthen the magnetic field.

  Since permeability varies depending on the metals and their alloys, the measuring instrument must be recalibrated every time the material is changed.

- Curved surfaces

  In practice, most measurement errors occur due to the shape of the sample: in curved surfaces the proportion of the magnetic field passing through the air is different.

  For example, if the meter is calibrated on a flat plate, the measurement on a concave surface would give a lower result, while on a convex would give a higher result. Errors that occur in this way increase a lot compared to their actual value.

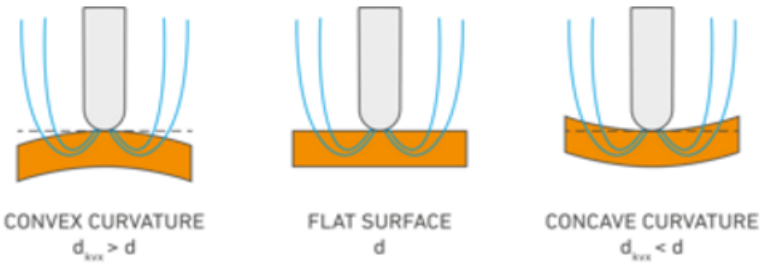

Figure 5.9 *Examples of measurements on different types of surfaces.*

- Small and flat components

  A similar effect can occur if the sample is small or very thin. Again, the magnetic field extends beyond the sample and into the air, systematically distorting the measurement results. To avoid these errors it's necessary to calibrate on an uncoated part corresponding to the final product.

- Roughness

  If the probe pole is positioned in a "valley" or on a "peak" of the roughness profile the result can be distorted. During these measurements the results vary greatly and it is advisable to repeat them several times to accumulate a stable average. In general, measures of coating thickness on rough surfaces are useful only if the coating is at least twice as thick as roughness peaks.

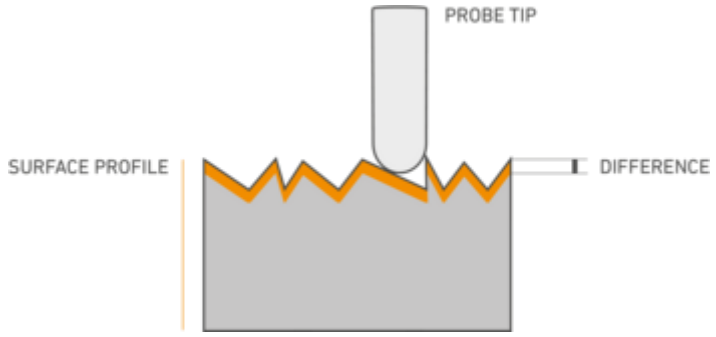

Figure 5.10 *Measurement of the content of ferrite on a rough surface.*

- Influence by the user

  Last but not least, the way the measuring instrument is used also plays an important role. Always ensure that the probe is positioned vertically and without pressure on the surface. For better accuracy, you can use a holder and automatically lower the probe to the sample. [8] [43]

5.2.5 Barkhausen Noise Test

Barkhausen Noise Analysis (BNA) is a non-destructive technique based on the inductive measurement of a noise-like signal generated in ferromagnetic material when introduced to an external magnetic field.

While the physical phenomenon of magnetic Barkhausen Noise was first observed and explained in 1919, industrial application of it as a measurement technique was uncommon before the 1980s. Today, BNA is a trusted method for stress analysis, material characterization and the detection of heat-treatment and other thermally induced material defects.

The materials which have ordered magnetic structure (ferro- and ferrimagnetic substances) contain fully magnetized regions called magnetic domains, in which all magnetic dipoles are aligned in the same direction.

The domains typically made up of 10^{12} to 10^{18} magnetic moments and are separated from each other by several hundred lattice parameter thick domain walls. When external magnetic field is applied or changed, the volume of the domains which have similar orientation to the direction of external field increases at the expanse of unfavourable aligned domains.

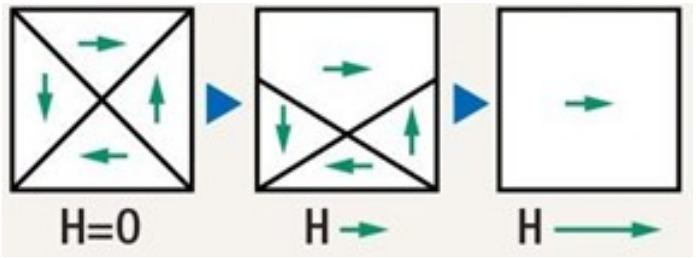

Figure 5.11 *Effect of the magnetic field applied on the magnetic domains.*

At the beginning of the magnetization curve the principal mechanism of magnetization is the motion of the domain walls.

In the irreversible domain wall displacement range the movement of domain walls is not continuous but it contains abrupt wall jumps.

In fact, the domain walls movements have a discontinuous speed due to their interactions with "pinning sites" formed by material discontinuities, grain boundaries, defects, inclusions and dislocations, which block domain walls motion, until there is enough external energy to overcome local energy barriers created by these imperfections in the crystal lattice.

An abrupt step, or "*Barkhausen jump*", then occurs in the magnetization curve. Domain walls then proceed to move through the material until encountering another pinning site. This process continues until the entire volume is magnetically aligned and has reached saturation, so the point where any further increase in applied field strength does not affect the net magnetization of the sample.

This sudden movements, characterized by discontinuities in the magnetization curve (as shown in Figure 5.12), can induce voltage pulses in a detector coil which is taken onto the surface or around the magnetized specimen.

The huge number of elementary domain wall jumps in a magnetizing cycle results a quasi-stochastic noise voltage called magnetic Barkhausen noise (BN).

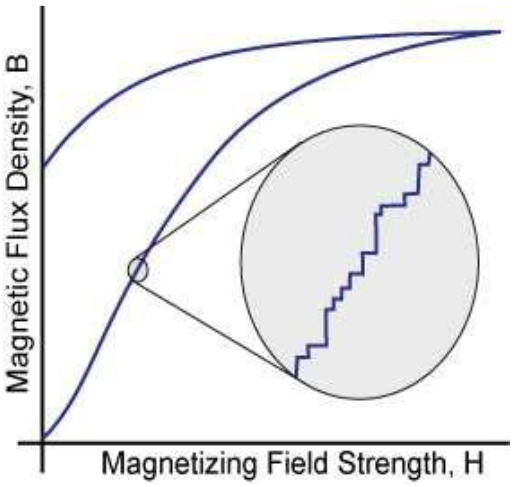

Figure 5.12 *Discontinuities (or "Barkhausen jumps") in the magnetization curve of the material caused by the interaction of the domain walls with the pinning sites.*

The quasi-stochastic BN contains a lot of information about the material and it can be characterized by different ways.

The most common solution is the signal Root Mean Square (RMS) value, described by the following equation.

$$x_{RMS} = \sqrt{\frac{1}{n}(x_1^2 + x_2^2 + \cdots + x_n^2)}$$

The Barkhausen noise is affected by material properties such as internal stress, microstructure, mechanical hardness and ferromagnetic phase.

In particular the last one allows to use this technique for controlling metallurgical processes which influence the amount of ferromagnetic phase; in fact, being the paramagnetic austenite associated with a lack of Barkenhausen noise, the emissions recorded using this technique can be directly linked with the content of ferromagnetic strain induced martensite in austenitic stainless steel.

Furthermore, the decrease of the pinning centers causes a diminution in the “jump events”, which lead to a smaller value of RMS recorded.

Naturally, the micromagnetic measurements have different limitations. The specimen must contain ferro- or ferrimagnetic phase. The penetration depth is relatively small (0.1-1 mm) depending on the applied excitation frequency. The accuracy of micromagnetic measurements strongly depends

on the air gap between the measuring head and the surface of the specimen (lift-off) and the behaviour of the surface layer.

The BN equipment, shown in Figure 5.13, utilised a 10 Hz sinusoidal exciting magnetic field produced by a function generator and a power amplifier applied to the specimen by a U-shaped magnetising coil perpendicular to the specimen's surface.

The applied measuring head contains then a pick-up coil perpendicular to the surface of the specimen, that is able to reveal little step changes in the induced magnetic field.

The signal of the pick-up coil was processed by a 0.3 kHz-38 kHz band pass filter, to ensure the elimination of the low frequency components, and amplified with a gain of 50 to give the proper amplitude to the signal and consequently improve the measurements resolution.

The applied sampling frequency was 100 kHz and the number of samples was 60˙000, with a sampling rate of 100˙000 S/s. For each sample was took one measurement for each side. [7] [8] [27] [28] [29] [36] [44]

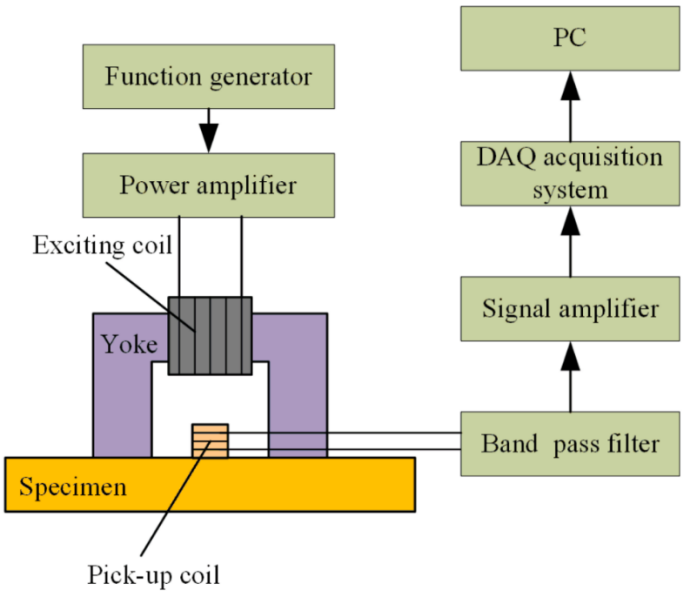

Figure 5.13 *Schematic illustration of the equipment used for the measurement of the Barkhausen noise.*

5.2.6 Förster Magnetometer

Forster test is an open circuit magnetic equipment used to reveal the real coercivity H_c value from the saturation hysteresis loop. It consists in a large solenoid coil which can produce 1000 A/cm magnetic field (enough to magnetize the present steel) and two magnetic sensors which sensitivity is very high (~1nT).

The idea of this equipment (Figure 5.14) is very simple and it is based to the definition of coercivity, so the intensity of the reverse magnetic field that it is necessary to apply to a material to cancel its magnetization after it has reached its saturation value

The specimen is put in the middle of a solenoidal coil and it's magnetized up to the saturation by a slow increasing of the excitation field. After that, this excitation field made by solenoid coil must be decreased slowly until H=0. The sample, containing some ferromagnetic phase, remains magnetize showing its own little magnetic field. The sensors, being the sample exactly perpendicular to them (a), are not able to measure the remanent magnetic field because the sensitivity direction of the sensors is perpendicular to the coil, and as long as the specimen remain in the middle of the coil, the perpendicular component will be zero.

Therefore, the second step (b) consists on move the sample horizontally in the coil until the sensors detect the maximum perpendicular component.

These two components have same direction but opposite signs, therefore, the signals revealed by the sensors are subtracted from each other in order to increase the sensitivity to the double.

The third step is, with the sample leaved in the point of maximum field detection, to change the polarity of the coil and to increase very slowly until the signal of the sensors become zero (sample demagnetization). The exciting field required corresponds to the coercive force H_c.

The coercivity stands for the ability of magnetic materials to resist demagnetization.

In the literature, for plastically deformed austenitic stainless steel AISI 304 there are two trends: H_c decreases with the increase of the volume fraction of martensite, while other studies report an increase in H_c with the increase of martensite.

This behaviour may be due to the interaction of magnetic domain walls with the martensite-austenite interfaces and the magnetostatic interaction between the martensite particles.

Therefore, H_c can be considered as an indicator of the size and distribution of the ferromagnetic martensite formed in the paramagnetic austenitic matrix.

In general, coercivity is related to the movement of the domain walls, which are affected by grain size and density of dislocations, which increases with deformation.

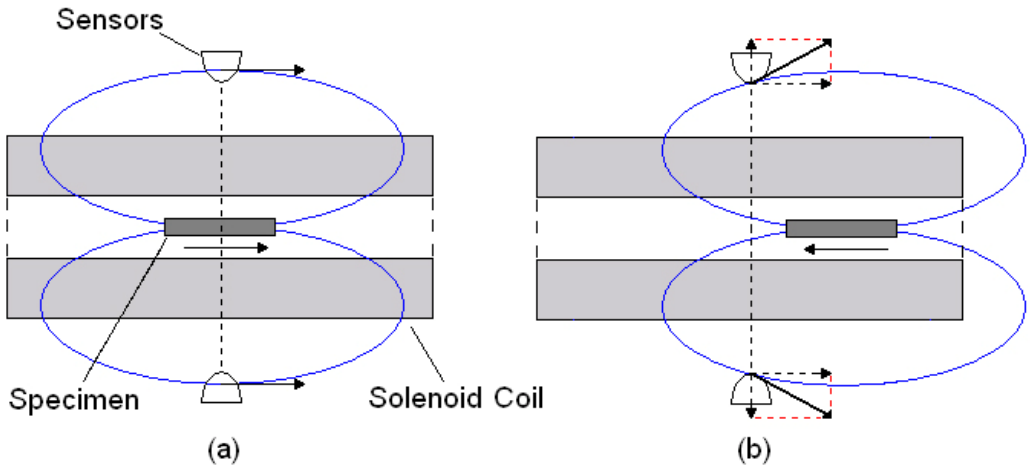

Figure 5.14 *Schematic illustration of the operating of the Förster magnetometer.*

This instrument take care also of the magnetic field of earth, that in some case could influence the measures. The earth magnetic field is about 50μT, fortunately in the case of this samples the saturation is much more, about 0.6T, so we worked in a range where there is no affection by earth magnetic field. Anyway, the system is tilted, to be in axis with the magnetic field of earth and there is two permanent magnet that can be settled to compensate this field.

Another consideration for this magnetic measurement can be done by distinguishing between *closed* and *open* circuit magnetic equipment (Figure 5.15).

The difference is that with close circuit magnetic equipment (a) the specimen touches the surface of magnetic poles, so there is no open space and the magnetic field lines can perfectly pass through the specimen bulk.

In this case the magnetic field inside the specimen is the same of the applied field:

$H_{in} = H_{out}$

Instead, in open circuit magnetic equipment (b), the absence of contact between specimen and poles surfaces could create some problems, because the field inside the material is different from the field applied field. It is possible to write:

$H_{in} = H_{out} - D \cdot M$

Where *M* is the magnetization of the sample and *D* is the demagnetization factor (depending on the geometry of the specimen).

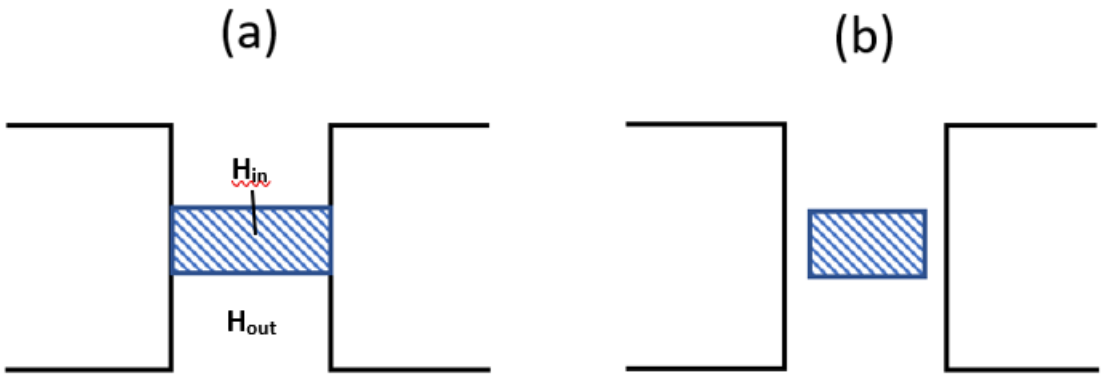

Figure 5.15 *Example of (a) closed and (b) open magnetic circuit.*

For example, with a long shape sample, the magnetic poles are distant from one other, and the demagnetizing effect is relatively low.

On the contrary, with small samples (e.g. a coin), the magnetic poles are very close to each other, therefore the demagnetization factor is very high and the field H_{in} inside the material will be zero. This means that with open circuit magnetic equipment long specimens must be used, to obtain values of H_{in} comparable to H_{out}.

If the sample is a cylinder of length *l* and diameter *d*, for *l/d* >8-10 the demagnetizing effect will be low and negligible. [7] [8] [30]

CHAPTER 6
Data analysis

As mentioned in the previous chapters, the analysis was carried out on three different types of materials: AISI 304 stainless steel, pure copper and CuZn alloys (CuZn15, CuZn30, CuZn33 and CuZn37).

These were rolled by varying the level of deformation and under different temperature conditions: at room temperature, at 100 °C and in liquid nitrogen.

Specifically, the deformation of the various samples, defined as ΔH [%], is shown in the graphs below.

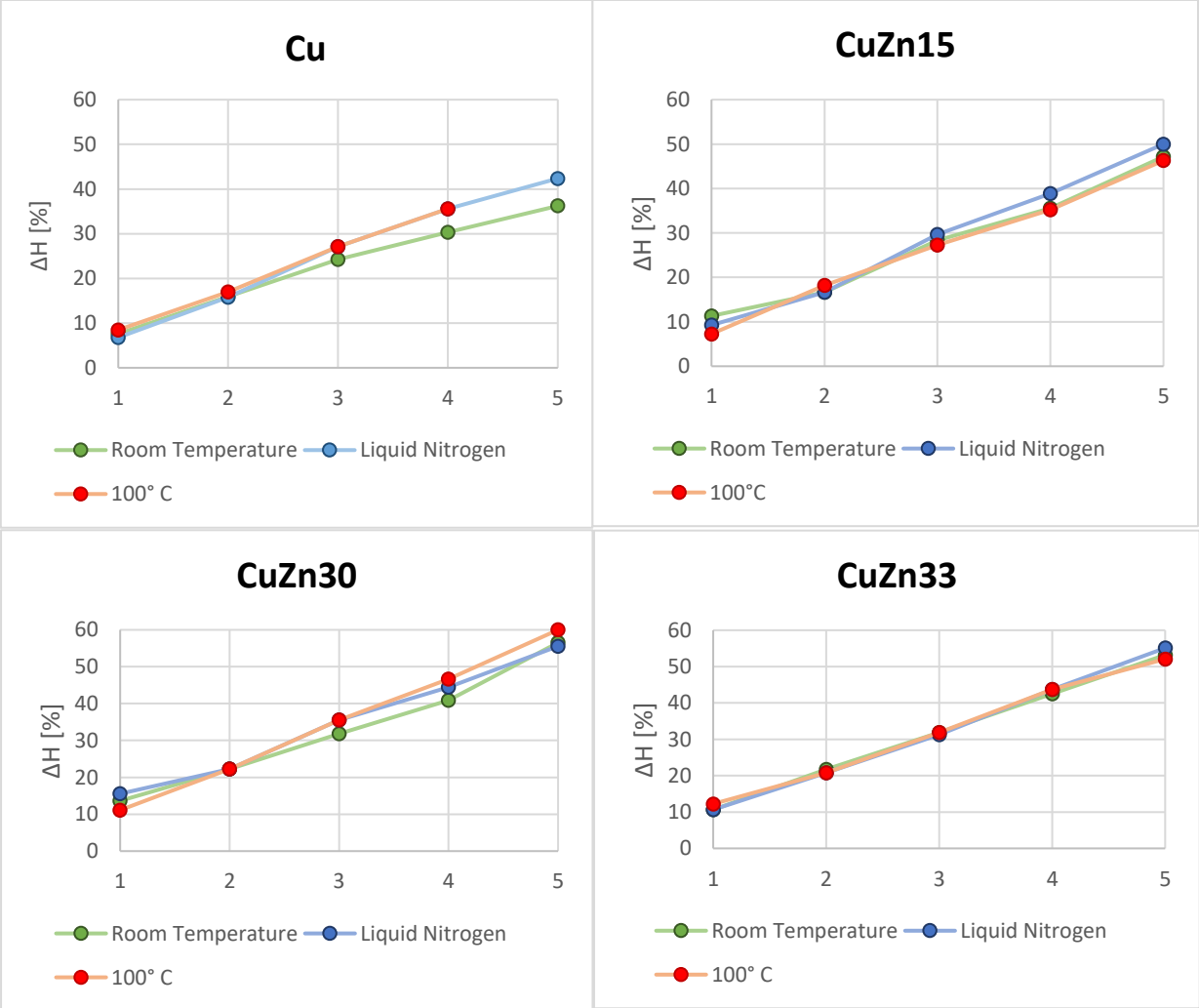

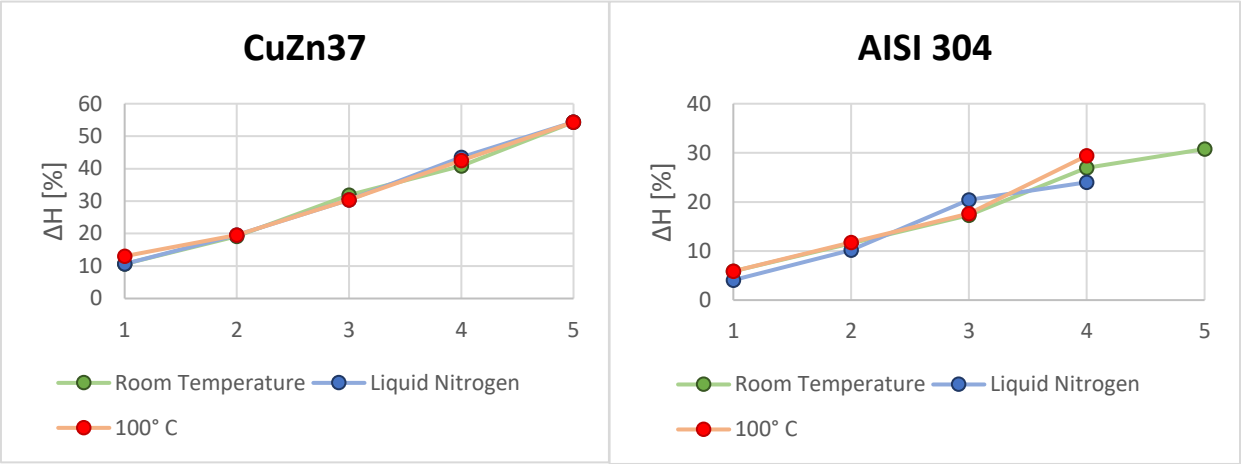

Figure 6.1 *Deformation comparison of the different samples reached in the materials at different conditions of temperature.*

Furthermore, the values obtained are also summarized numerically in the Table 6.1.

Table 6.1 *ΔH [%] e Δarea [%] obtained in the samples after rolling at different temperatures.*

Material	Sample	Room Temperature		Liquid Nitrogen		100°C	
		ΔH [%]	Δarea [%]	ΔH [%]	Δarea [%]	ΔH [%]	Δarea [%]
Cu	1	7,58	6,81	6,78	5,29	8,47	6,81
	2	15,94	13,19	15,79	13,63	16,95	14,86
	3	24,24	20,58	27,12	24,37	27,12	23,41
	4	30,30	26,10	35,59	31,74	35,59	30,60
	5	36,23	33,66	42,37	39,52	-	-
CuZn15	1	11,32	9,75	9,26	5,29	7,27	6,50
	2	16,67	14,41	16,67	13,63	18,18	16,64
	3	28,30	25,29	29,63	24,37	27,27	24,83
	4	35,59	32,82	38,89	31,74	35,19	31,77
	5	47,17	44,83	50,00	39,52	46,30	41,98
CuZn30	1	13,64	12,91	15,56	12,74	11,11	9,64
	2	22,22	18,95	22,22	18,33	22,22	19,61
	3	31,82	28,98	35,56	31,83	35,56	32,33
	4	40,91	37,43	44,44	40,77	46,67	43,11
	5	56,52	53,60	55,56	51,48	60,00	56,67
CuZn33	1	10,64	9,90	10,64	9,16	12,24	10,78
	2	21,74	19,15	20,83	17,53	20,83	18,22
	3	31,91	29,10	31,25	28,43	31,91	29,08
	4	42,55	39,20	43,75	40,00	43,75	40,96
	5	53,19	50,07	55,10	51,36	52,08	48,89

Material	Sample	Room Temperature		Liquid Nitrogen		100°C	
		ΔH [%]	Δarea [%]	ΔH [%]	Δarea [%]	ΔH [%]	Δarea [%]
CuZn37	1	10,64	9,14	10,64	8,40	13,04	12,33
	2	19,15	17,16	19,57	16,91	19,57	17,57
	3	31,91	28,54	30,43	27,58	30,43	28,14
	4	40,82	36,45	43,48	40,70	42,55	39,68
	5	54,35	50,54	54,35	51,73	54,35	50,95
AISI 304	1	5,88	4,61	4,08	3,93	5,88	4,49
	2	11,54	10,36	10,20	8,91	11,76	9,71
	3	17,31	16,10	20,41	18,12	17,65	15,67
	4	26,92	24,07	24,00	21,27	29,41	26,85
	5	30,77	26,84	-	-	-	-

6.2 OM Analysis

For the copper and the CuZn the etching of the samples and the following analysis with an optical microscope allowed the detection of the twin boundaries created during the deformation.

To quantify their presence and investigate the effect of the rolling temperature and composition it was decided to introduce the density ϕ [μm^{-1}], which corresponds to the ratio of the sum of the lengths of the twinning and the area of the micrography.

The correlation with the composition is shown graphically in Figure 6.2.

(a)

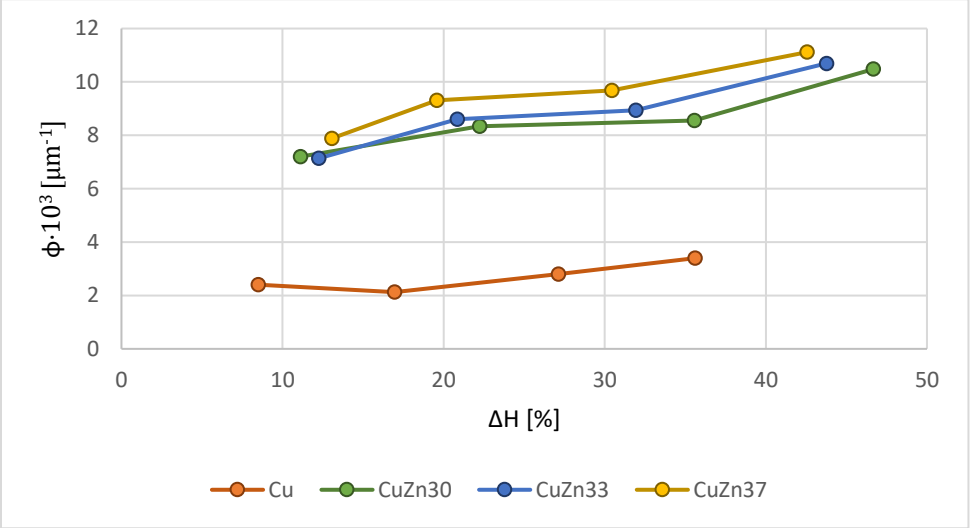

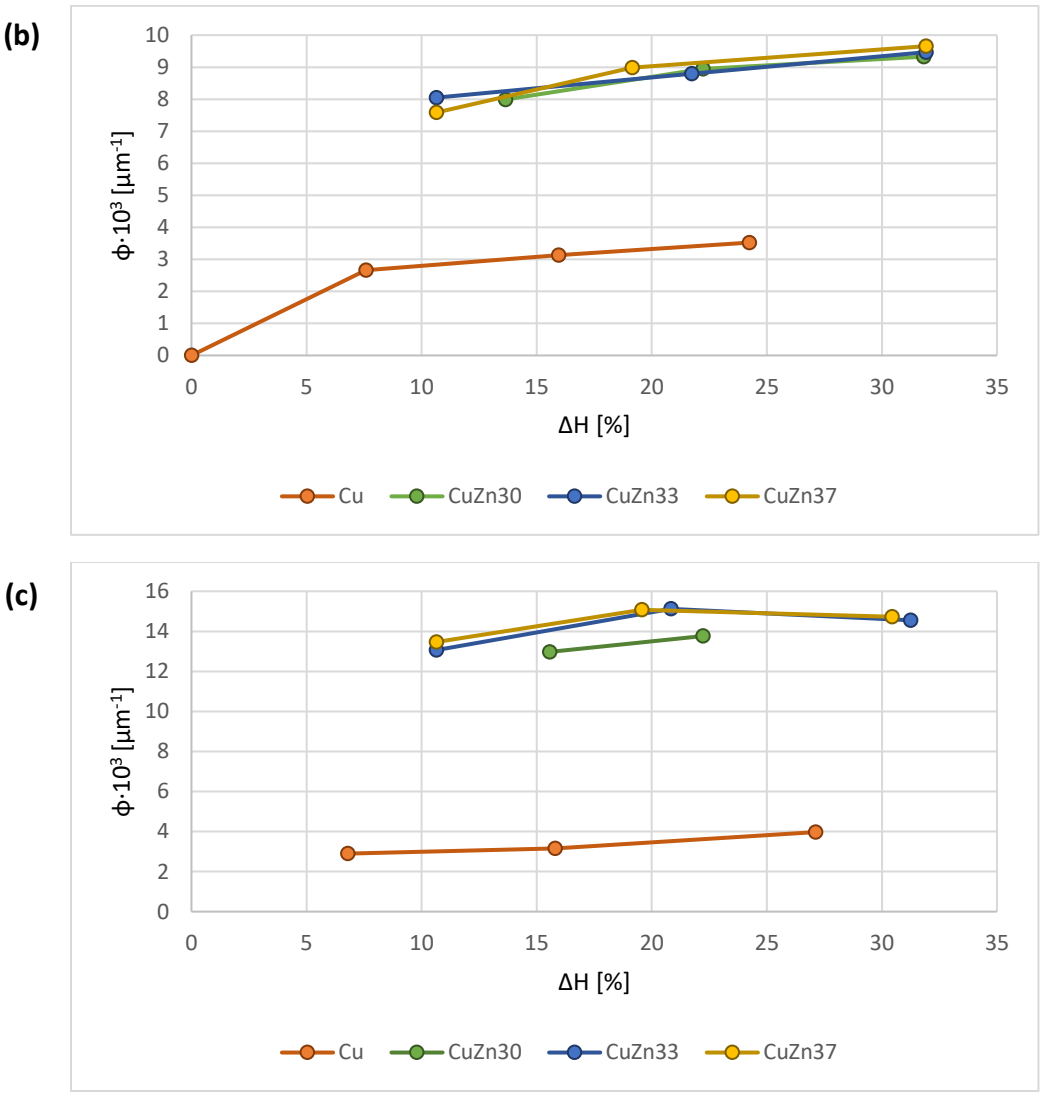

Figure 6.2 *Density of twin boundaries for different compositions at (a) 100° C, (b) room temperature and (c) in liquid nitrogen.*

It's possible to see that at each rolling temperature the zinc tends to increase the density of the twin boundaries. This is evident comparing the pure copper (which starts from a density equal to zero in the sample 0, so not deformed, at room temperature) to the alloys, but also considering only the brasses an increase in the zinc content generally corresponds to a slight increase in the number of twin boundaries.

Note that not in all the sample was possible to analyse the density: at high level of the deformation, especially at low temperatures, the grain become to distorted to obtain a clear microscopy, also

after several etching steps, so the detection of the twinning resulted too difficult to obtain reliable data.

This could be the explanation of the decrease of ϕ in the samples rolled in liquid nitrogen at high deformation.

Furthermore, notice that the CuZn15 wasn't included in the analysis because after rolling it tended to assume a particular microstructure, which made it particularly difficult to distinguish the twinnings from grains distorted by dislocations.

An example is reported in Figure 6.3.

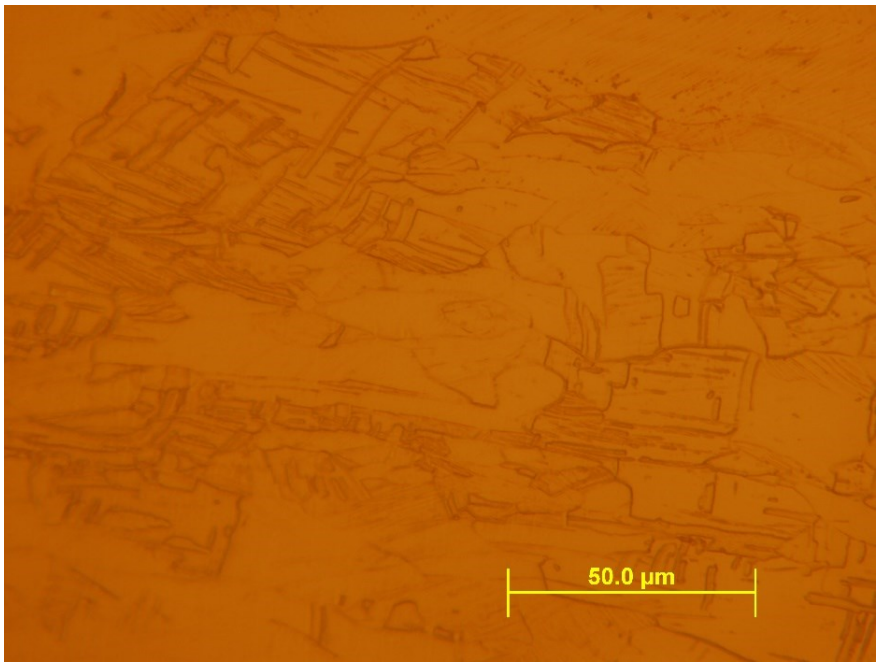

Figure 6.3 *Micrography of the sample 3 of CuZn15 rolled at 100°C.*

To investigate also the effect of the temperature it was decided to use an average value of ϕ between all the samples of the same compositions, associated to an average value of deformation ΔH.

The results are shown in Figure 6.4.

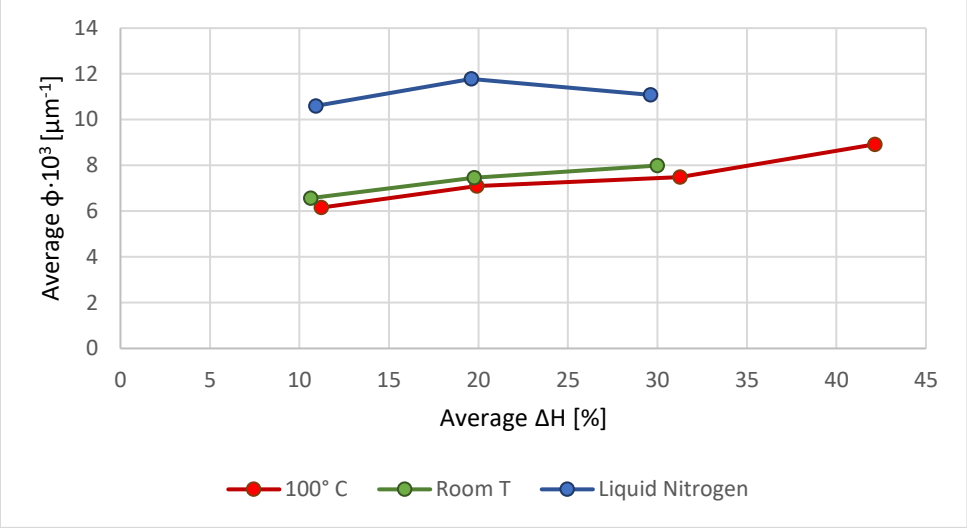

Figure 6.4 *Average density of dislocations measured at different temperatures in function of the average deformation level.*

It is evident that a decreasing in the rolling temperature has a positive effect on the density of the twin boundaries, with higher values of the average ϕ measured in the samples rolled in liquid nitrogen.

In particularly, for the curve of these specimens it's possible to observe a decrease in the value for the last deformation level, due to the fact that there were just two samples of CuZn30 analysable so the lower density of pure copper assumes a bigger weight in the calculation of the average.

Furthermore, as said before, for high level of deformation the detection of the twinning becomes more difficult due to the distortion of the grain, so the data could be not totally reliable.

6.2 Vickers Hardness Test

KB Pruftechnik Hardness Tester was used for the experimental measurements of the AISI 304 stainless steel, working with a load of 30 Kg and an application time of 12 seconds.

For each sample 5 measurements in different point of the surface were taken, reporting in the end the average value obtained.

The values obtained are reported in Table 6.2 and a graphically comparison of the average hardness is made in Figure 6.5.

Table 6.2 *Vickers Hardness measured in AISI 304 samples rolled at different temperatures.*

Rolling temperature	Sample	Measurements [HV]					Vickers Hardness [HV]
		1°	2°	3°	4°	5°	
Room Temperature	1	247	242	246	246	249	**246.00**
	2	260	258	261	259	257	**259.00**
	3	282	282	277	279	280	**280.00**
	4	292	291	292	292	294	**292.20**
	5	335	333	333	336	336	**334.60**
100°C	1	262	262	263	261	263	**262.20**
	2	279	278	279	279	279	**278.80**
	3	288	293	292	293	294	**292.00**
	4	331	334	331	330	329	**331.00**
Liquid Nitrogen	1	260	261	260	261	260	**260.40**
	2	286	279	286	282	281	**282.80**
	3	314	315	310	314	317	**314.00**
	4	347	352	355	349	352	**351.00**

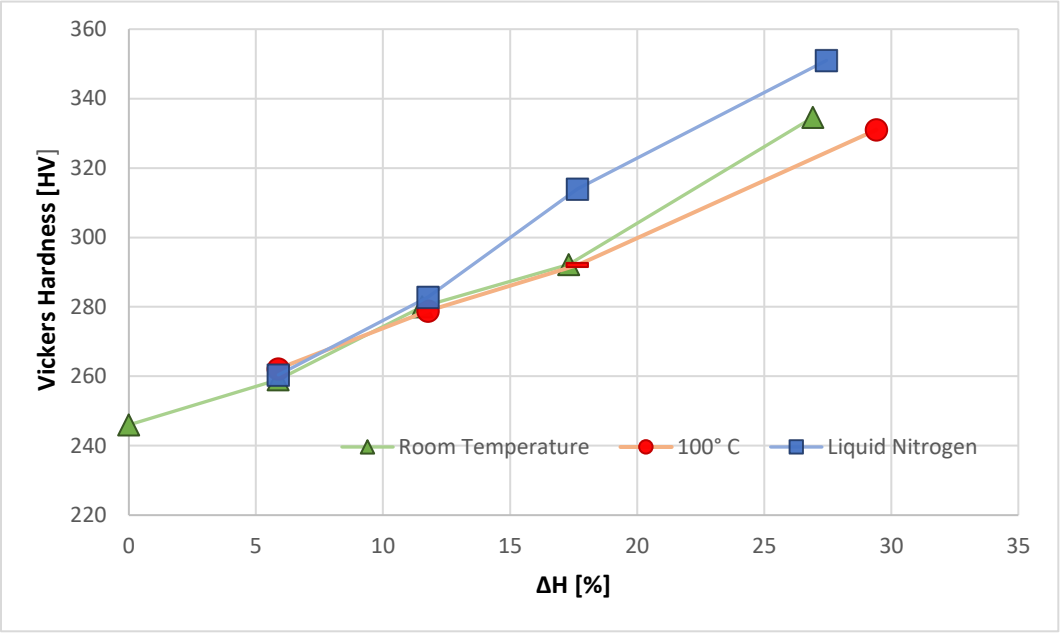

Figure 6.5 *Comparison of the Vickers Hardness of the AISI 304 samples rolled at different temperatures in function of their deformation level.*

It is evident from the graph that the most deformed specimens have higher hardness characteristics, in particular the effect is more accentuated with lower rolling temperatures.
It should be specified that the sample number 3 rolled at 100°C was too bended to have a perfect measurement so the value obtained could be not totally reliable.

6.3 Ferrite Tester

The ferrite content was inspected in stainless steel AISI 304 samples, using a *Feritscope FMP30* by *Fischer*®.
For each specimen 10 measurements were taken (five on each side), to have a reliable average value of the ferromagnetic phase present in the material.
The results, reported as the average value of the content of ferrite [%] are shown in Table 6.3.

Table 6.3 *Average values of content of ferrite [%] measured in AISI 304 samples rolled at different temperatures.*

Rolling Temperature	Sample	ΔH [%]	Content of ferrite [%]
Room temperature	1	5,88	0,29
	2	11,54	0,53
	3	17,31	0,88
	4	26,92	2,13
100°C	1	5,88	0,25
	2	11,76	0,27
	3	17,65	0,45
	4	29,41	1,19
Liquid Nitrogen	1	5,88	1,33
	2	11,76	7,02
	3	17,65	9,06
	4	27,45	10,93

To understand in an easier way the effect of the rolling temperatures on the samples, the values of the ferrite content measured are also shown in a graph in function of the deformation level (Figure 6.6).

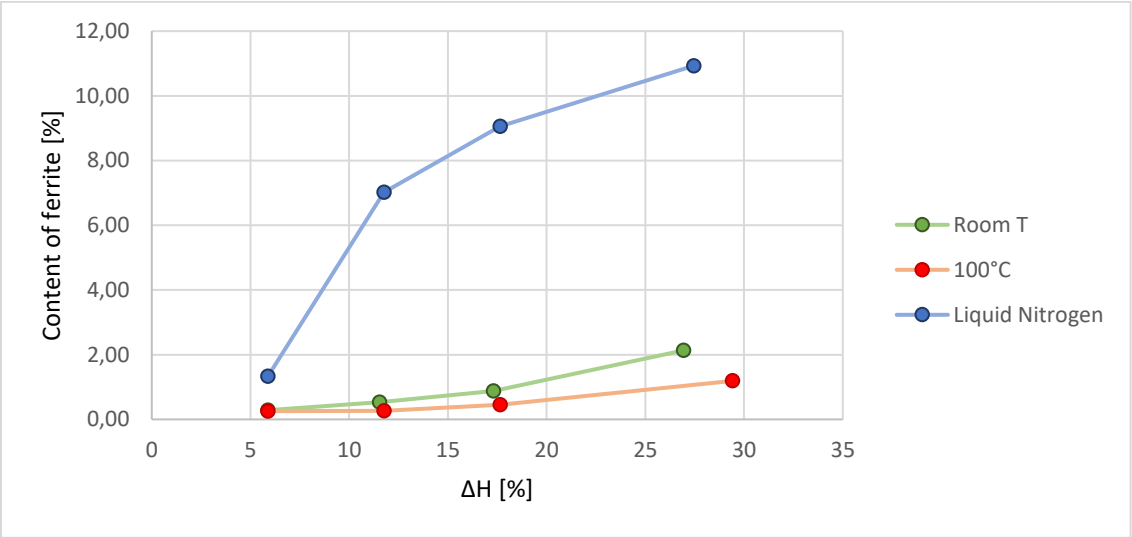

Figure 6.6 *Content of ferrite [%] measured in the samples rolled at different temperatures in function of their deformation level.*

It was noticed that in the samples rolled in liquid nitrogen the content of ferrite changed significantly along the length of the specimens, probably due to a not perfect homogenization of the temperature during the rolling.

For this reason, the measurement was done considering only the part of the sample with the highest content of ferrite (excluding the ends), which was supposed to be colder during the rolling operation.

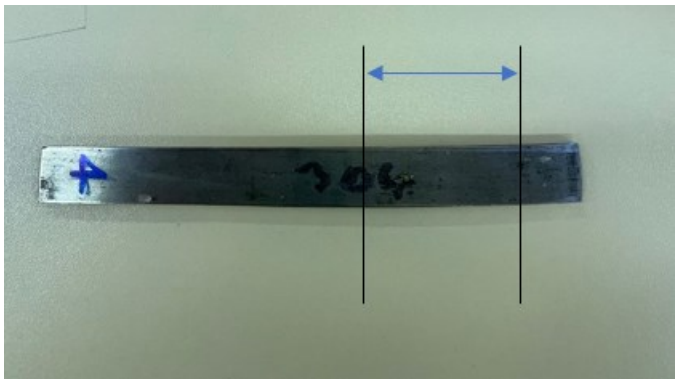

Figure 6.7 *Part of the sample subjected to the measurement.*

To obtain more realistic results a second set of short samples, described in Table 6.4, was prepared and rolled with the liquid nitrogen, paying more attention at reaching the right temperature in the entire specimen.

In terms of content of ferrite, the results showed the same trend but higher values (constant along the length), that probably means that the initial temperature reached before rolling was lower.

Table 6.4 *Content of ferrite [%] measured in the second set of AISI 304 samples rolled in liquid nitrogen.*

Sample	Content of ferrite [%]										Average	ΔH
	1°	*2°*	*3°*	*4°*	*5°*	*6°*	*7°*	*8°*	*9°*	*10°*	[%]	[%]
1	2.10	2.10	2.20	2.20	2.30	2.00	2.10	2.30	2.20	2.30	**2.18**	**4.08**
2	14.70	14.60	14.50	14.40	14.80	15.30	14.30	13.20	13.40	13.70	**14.29**	**10.20**
3	23.40	24.20	24.00	24.10	24.20	23.80	24.00	24.00	24.30	23.80	**23.98**	**20.41**
4	22.00	22.00	21.40	21.50	21.50	22.70	22.90	23.20	23.80	23.30	**22.43**	**24.00**

The graphic comparison between the two sets of samples rolled in liquid nitrogen is made in Figure 6.7.

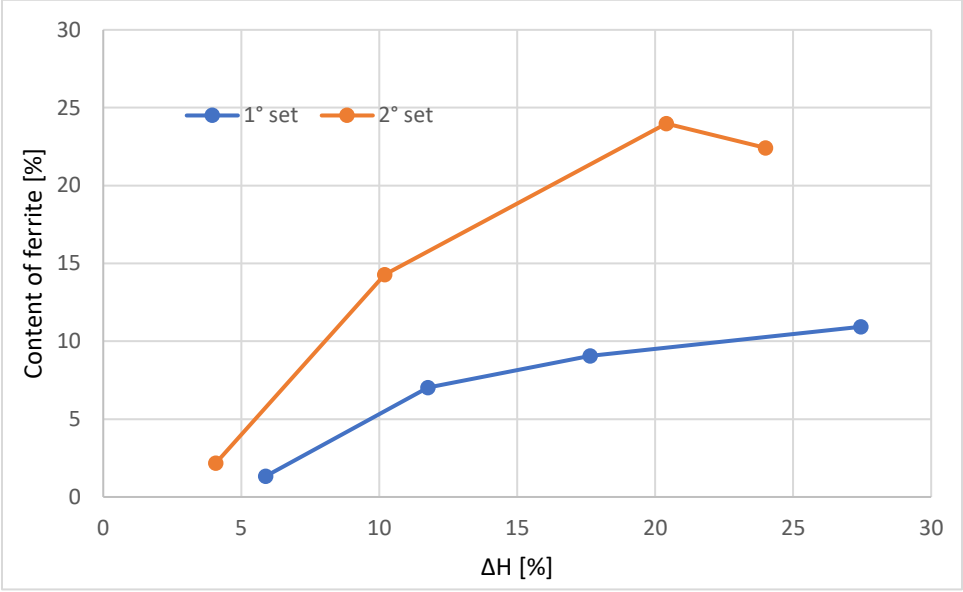

Figure 6.7 *Content of ferrite [%] of the samples of the two sets rolled in liquid nitrogen at different deformations.*

In general, it can be seen that an increase in the level of deformation corresponds to an increase in the ferrite content measured by the instrument. with a greater increase as the temperature decreases. The graphs show that the trend is very similar at room temperature and at 100 ºC, while at low temperatures it's possible to see an initial massive increase of martensite followed by a sightlier growing at higher deformation.

6.3 Barkhausen Noise Test

The Barkhausen effect was tested using an instrument built within the BME University of Budapest.

The results were characterized as the *Root Mean Square (RMS)* of the signal. in particular using the average value of the two measurements made for each sample (one per side).

The values obtained for AISI 304 stainless steel are shown in the Table 6.5.

Table 6.5 *Values of the Root Mean Square obtained for AISI 304 samples rolled at different temperatures.*

Rolling Temperature	Sample	RMS [mV]		Average RMS	ΔH [%]
		1°	2°		
Room temperature	1	12.00	12.00	12.00	5.88
	2	12.00	16.00	14.50	11.54
	3	18.00	16.00	17.00	17.31
	4	20.00	20.00	20.00	26.92
100°C	1	8.00	8.00	8.00	5.88
	2	10.00	10.00	10.00	11.76
	3	15.00	15.00	15.00	17.65
	4	16.00	16.00	16.00	29.41
Liquid Nitrogen	1	21.00	16.00	18.50	5.88
	2	47.00	51.00	49.00	11.76
	3	189.00	209.00	199.00	17.65
	4	278.00	244.00	261.00	27.45

To have a better visualization of the data. these have been graphically reported in Figure 6.8.

It is clear that rolling at low temperature conditions (liquid nitrogen) has led to a significant increase in the signal recorded compared to higher temperatures.

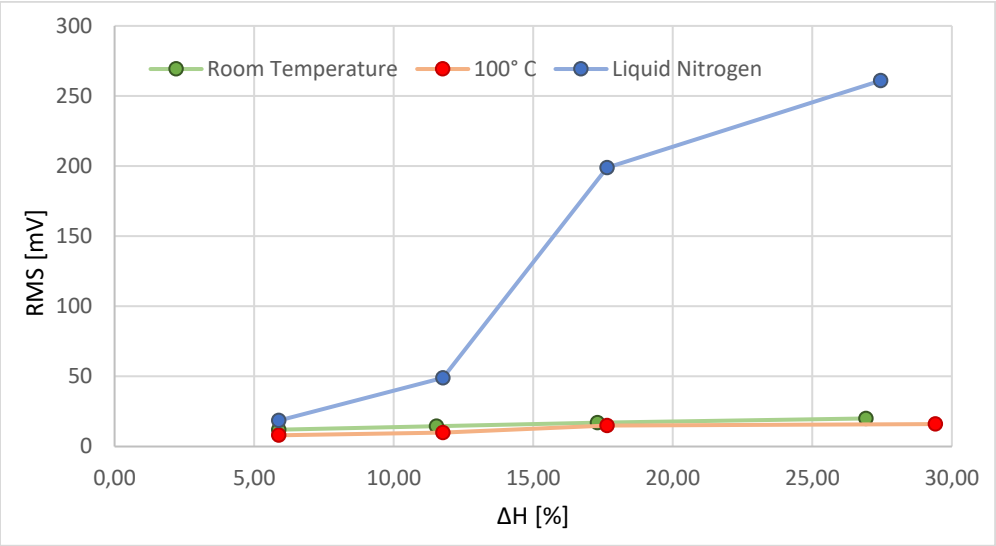

Figure 6.8 *RMS measured in AISI 304 samples rolled at different temperatures in function of their deformation.*

Specifically. it was decided to report separately the data obtained with the samples rolled at 100 ºC and at room temperature to facilitate the comparison (Figure 6.9).

Again. the effect of the drop in temperature has led to an increase in the signal (although less noticeable than the specimens rolled in liquid nitrogen) but, despite this, the two trends present a similar shape.

(It should be remembered that the sample number 3 rolled at 100°C was too bended to have a perfect measurement so the value obtained could be not totally reliable.)

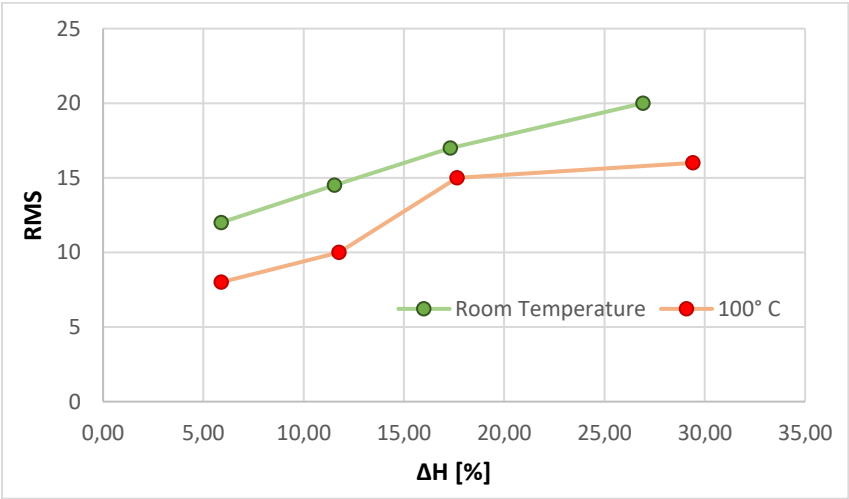

Figure 6.9 *Comparison of the RMS between AISI 304 samples rolled at room temperature and at 100°C.*

6.4 Förster Magnetometer

For each AISI 304 sample, the mean value of the coercivity H_c obtained from the two measurements (one per polarity) is reported.

The results are shown in Table 6.6.

Table 6.6 *Coercivity H_c [A/cm] measured in AISI 304 samples rolled at different temperatures.*

Temperature	Sample	H_c [A/cm]		Average H_c	ΔH [%]
		1°	2°		
Room temperature	1	2.00	12.00	**7.00**	**5.88**
	2	8.00	16.00	**12.00**	**11.54**
	3	12.00	22.00	**17.00**	**17.31**
	4	29.00	38.00	**33.50**	**26.92**
100°C	1	1.00	10.00	**5.50**	**5.88**
	2	1.00	11.00	**6.00**	**11.76**
	3	6.00	16.00	**11.00**	**17.65**
	4	12.00	23.00	**17.50**	**29.41**
Liquid Nitrogen	1	8.00	34.00	**21.00**	**5.88**
	2	48.00	62.00	**55.00**	**11.76**
	3	54.00	64.00	**59.00**	**17.65**
	4	58.00	64.00	**61.00**	**27.45**

In Figure 6.10 it is possible to notice graphically how once again the effect of the rolling temperature is very significant.

Specifically, there is an increase in the coercivity recorded in the samples worked at lower temperatures, associated with the presence of greater ferromagnetic phase.

The trends of the specimens rolled at room temperature and at 100°C show a similar shape, instead (as noticed in previous analysis) the coercivity in function of the deformation value for the cold rolled samples presents a huge initial increase, followed by a stabilization of the value.

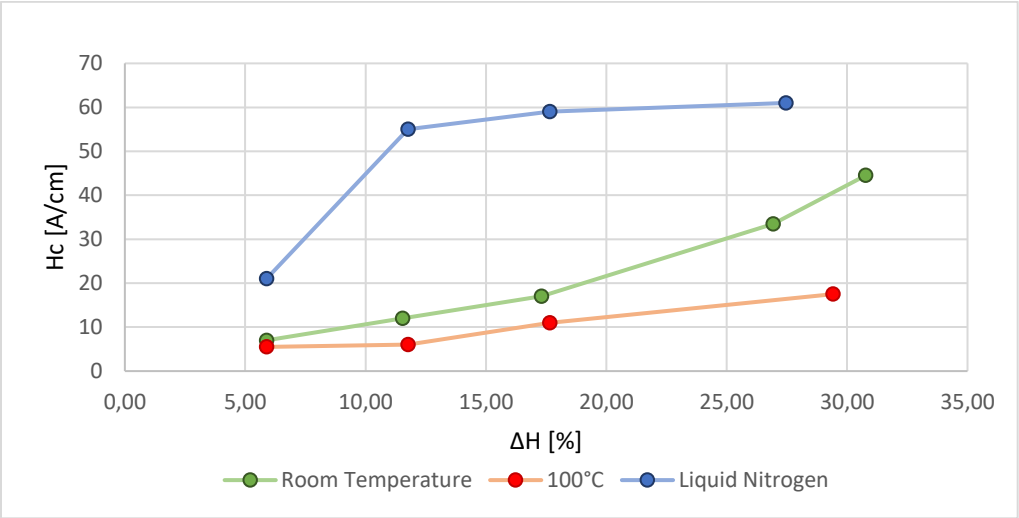

Figure 6.10 *Comparison of the coercivity H_c [A/cm] measured in AISI 304 samples rolled at different temperature in function of their deformations.*

The analysis was repeated for the second set of samples rolled in liquid nitrogen, characterized by a smaller length.

The results obtained are shown in Table 6.7.

Table 6.7 *Coercivity Hc [A/cm] measured in the second set of AISI 304 samples.*

Sample	**Hc [A/cm]**		**Average H_c [A/cm]**	**ΔH [%]**
	1°	*2°*		
1	21.00	12.00	16.50	4.08
2	38.00	32.00	35.00	10.20
3	33.00	28.00	30.50	20.41
4	33.00	35.00	34.00	24.00

Comparing in Figure 6.11 the two sets of specimens processed in low temperature condition, it's possible to notice that the curves have a similar shape but the values obtained with the second set (short samples) are less than those of the first (long samples).

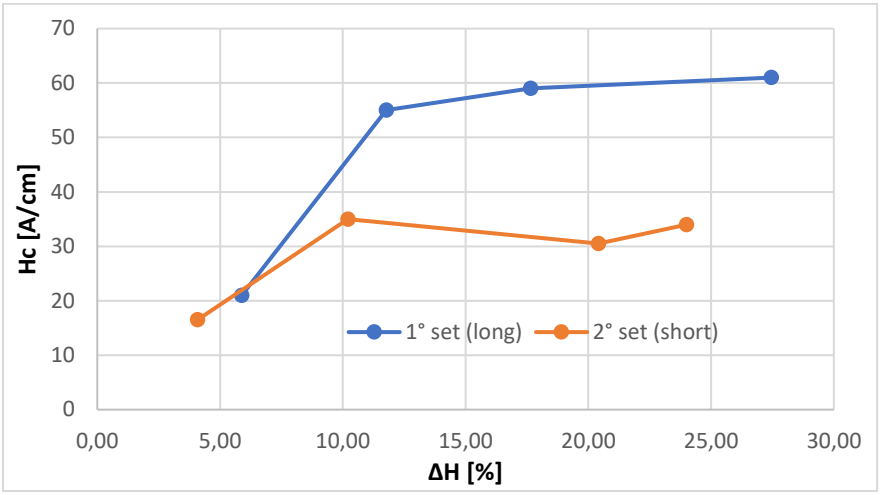

Figure 6.11 *Comparison of the coercivity H_c [A/cm] measured in the two sets of AISI 304 samples.*

This is probably due to the smaller length of the samples belonging to the second set, which doesn't allow to obtain the condition of close magnetic circuit.

In this case the ratio l/d is certainly smaller than 8, so the effect of the demagnetization factor D becomes significant in the analysis and lead to smaller values of the coercivity H_c.

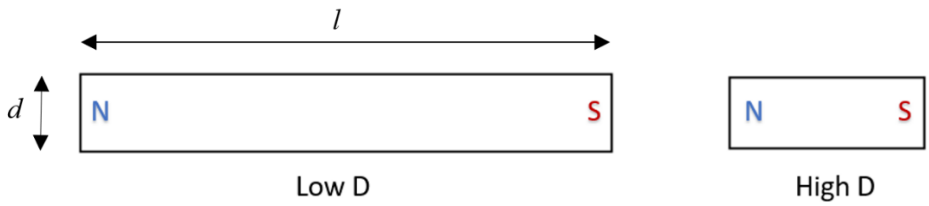

Figure 6.10 *Effect of the ratio l/d on the demagnetization factor D.*

CONCLUSIONS

From the analyses and the measurements carried out on the AISI 304, copper and CuZn alloys samples it's possible to summarize the results obtained and get some considerations.

- In the pure copper and CuZn alloys it was tried to find a rough correlation between the Stacking Fault Energy of the samples, the composition and the rolling temperature trough the detection of the twin boundaries formed during the deformation.

  From the OM analyses results that the parameter ϕ chosen for the quantification of the presence of the twinning generally increase with an increasing in the content of zinc with an almost linear relationship with the deformation ΔH.

  This means that the zinc in the alloying contributes to decrease the SFE, changing the mechanism of deformation from the dislocation glide to twinning.

  A similar trend can be observed also investigating the effect of temperature: here the increase in the rolling temperature causes a decreasing in the density of the twin boundaries, witnessed from the higher values of ϕ obtained from the samples rolled in liquid nitrogen.

  Also in this case the decreasing in temperature tends to decrease the SFE and so to favour the formation of twinning.

- In the AISI 304 samples the rolling process creates strain induced martensite in the steel: this is easily detectable from the measurements of the content of ferrite, which give a rough indication on the ferromagnetic phase present in the samples.

  From the structural point of view there is an increase in term of volume of the new phase that puts other pressure on the close austenite and promotes the formation of new martensite ("*positive feedback*").

  This phenomenon would seem to explain the shape of the curves Content of ferrite [%] vs ΔH [%] at room temperature and at 100°C, which show an increasing trend.

  Instead, in the curve of the samples rolled in liquid nitrogen it's possible to see a different trend with an initial massive increase of ferromagnetic phase followed by a sightlier growing at higher deformation.

That could be explained assuming that in a multi-step rolling the temperature of the sample increases during the process so at higher deformation the specimen isn't at 77 K (or close) anymore and the effect of the temperature becomes less significant.

Another possible explanation could be that at low temperature the yield strength of the steel becomes higher so the stress induced by the increasing volume of the martensite could be not enough to reach plastic deformation and so to induce a new martensite formation.

Further investigations are needed to find the real reason.

In conclusion, an increasing of the deformation level and a decreasing of the rolling temperature lead to a lower Stacking Fault Energy in the specimens, so the deformation mechanism through martensitic transformation becomes increasingly favoured.

Being martensite a hard and ferromagnetic phase so it's possible to note that the results obtained with the Vickers Hardness, Förster and Barkenhausen tests are coherent with the content of ferrite (approximate indicator of martensite) measured in the samples.

In particular, the Barkhausen noise test shows that the RMS recorded increases with the deformation applied, and its evolution is mainly driven by the increasing fraction of the ferromagnetic phase embedded in the paramagnetic austenite.

Also, the increasing in the deformation level causes a bigger density of dislocations (which can be considered as pinning centers for the domain walls) and therefore a rise in the number of "jump events" linked with the RMS value measured.

Furthermore, to explain the increase of the coercivity it's possible to assume that in a first moment the rise in the dislocation density plays a dominant role; after this initial stage, the martensitic transformation increases the ferromagnetic phase in the sample and consequently the magnetic domain walls, as well as increasing the interface with the austenitic phase (which is able to act as strong anchoring site).

Finally, the increased hardness is thought to be the effect of the increased dislocation density, the austenite strain hardening, the possible grain refinement and the increasing amount of strain induced martensite transformation (and therefore the presence of a much harder phase).

Nomenclature

(…) = crystallographic plane

<…> = crystallographic direction

Ms = temperature at which during quenching the remaining austenite begins to transform into martensite

Rm = maximum stress [N/mm^2]

Rs = yield stress [N/mm^2]

$R_{p\ (0.02\%)}$ = 0.02% proof stress [N/mm^2]

A = elongation [%]

A_5 = elongation in specimens with L_0/d_o equals to 5 [%]

FCC = face-centered cubic

BCC = body-centered cubic

HCP = hexagonal closed packed

HB = Brinell Hardness

HV = Vickers Hardness

w_0 = initial width of the sample [mm]

w_i = width of the sample after the rolling process [mm]

h_0 = initial thickness of the sample [mm]

h_i = thickness of the sample after rolling process [mm]

$Area_o$ = initial section of the sample [mm^2]

$Area_i$ = section of the sample after rolling process [mm^2]

l_i = length of the twin boundary [μm]

A = area of the micrography [μm^2]

ϕ = twin boundaries "density" [μm^{-1}]

H = magnetic field applied [A·m]

B = field generated into the material after the application of H [T]

μ_0 = vacuum permeability [H·m]

M = magnetization [A·m]

μ_r = relative magnetic permeability

χ_m = magnetic susceptibility

H_c = coercivity [A/cm]

RMS = Root Mean Square

References

[1] Montanari, R., Baricco, M., & Angella, G. (2005). *Tecniche sperimentali per la caratterizzazione dei materiali. Dal laboratorio alla produzione*.

[2] Mazzoldi, P., Nigro, M., & Voci, C. (2008). *Elementi di fisica. Elettromagnetismo e onde*.

[3] Paolucci, G. M. (1998). *Appunti di materiali metallici per il corso di chimica e materiali: diploma in ingegneria meccanica*.

[4] Paolucci, G. M. (2000). *Lezioni di metallurgia Vol.1. Struttura, proprietà e comportamento dei materiali metallici.*

[5] Paolucci, G. M. (1995). *Lezioni di metallurgia Vol.2. Tecnologia dei materiali metallici.*

[6] Paolucci, G. M. (1996). *Lezioni di metallurgia Vol.3. Analisi, prove e controlli sui materiali metallici.*

[7] Fassina, G. (2010). *Effects of cold rolling on austenite to α'- martensite transformation in 2101 lean duplex stainless steel*. Tesi di laurea in Ingegneria dei Materiali, Università di Padova.

[8] Bianchi, M. (2011). *Effects of cold rolling on phase precipitation and phase transformation in a 2507 SDSS*. Tesi di laurea in Ingegneria Meccanica, Università di Padova.

[9] Del Grosso, A. (2020). *Effects of nitrogen and heat treatments on the thermoelectric power, magnetic and hardness properties of C75 high carbon steel.* Tesi di laurea in Ingegneria dei Materiali, Università di Padova.

[10] Todesco, A. (2016). *Effects of heat treatment and cold rolling on kinetics of ferrite decomposition processes in DDS 2507*. Tesi di laurea in Ingegneria dei Materiali, Università di Padova.

[11] Olsson, M. (2014). *Thermodynamic Modeling of the Stacking Fault Energy in Austenitic Stainless Steels.* Degree project in Thermodynamic Modeling, KTH Royal Institute of Technology.

[12] Saleh, A. A. (2012). *Recrystallisation and deformation behaviour of Twinning Induced Plasticity (TWIP) steel.* Thesis in Mechanical, Material and Mechatronic Engineering, University of Wollongong.

[13] Bleck, W., & Haase, C. (2019). *Physical Metallurgy of High Manganese Steels*. MDPI.

[14] Mészáros, I., Kaldor, M., & Hidasi, B. (1996). *Barkhausen Noise Energy Measurement Method for Characterizing the Ferromagnetic Ratio of Alloys*. Materials Science Forum, vols. 210–213, pp. 31–38.

[15] Mészáros, I. (2003). *Micromagnetic Measurements and their Applications*. Materials Science Forum, vols. 414-415, pp. 275-280.

[16] Jiles, D. C. (1998). *Introduction to Magnetism and Magnetic Materials*, 2nd Edition. CRC Press.

[17] International, A., & Society, I. M. (1986). *Guide to Materials Engineering Data and Information.* (RAME+brass)

[18] West, E. G. (1979). *The Selection and Use of Copper-based Alloys*. Oxford University Press, Oxford, UK.(rame)

[19] ASM International (2001). *Alloy Finder*, 3rd Edition. (rame+brass+steel)

[20] Robb, C. (1987). *Metals Databook*. (BRASS)

[21] Bringas, J. E., & Wayman, M. L. (2003). *CASTI Metals Black Book: North American ferrous data.* Casti Pub.(brass)

[22] Nickel Development Institute (1994). *Stainless Steels: A Guide to Stainless Steels*.

[23 UK Steel Association (1994). Iron and Steel Specifications, 8th Edition.

[24] Woolman, J. & Mottram, R. A. (1966). *The Mechanical and Physical Properties of the British Standards En Steels*. Pergamon Press, Oxford.

[25] Ghosh, A., & Chatterjee, A. (2008). *Ironmaking and Steelmaking: theory and practice*. PHI Learning Pvt. Ltd.

[26] Lv, X., Sun, L., & Sun, L. (2023). *Study on Magnetic Properties of Ferromagnetic Materials in Cryogenic Conditions.* Cryogenics, 103643.

[27] Ortega-Labra, O., Martínez-Ortiz, P., Manh, T. L., Velazquez-Lozada, E., & Perez-Benitez, J. A. (2022). *What does a Barkhausen surface coil actually measure?* Journal of Magnetism and Magnetic Materials, 169938.

[28] Neslušan, M., Bronček, J., Minárik, P., Čapek, J., Vicen, M., & Drbúl, M. (2022). *Friction and wear of AISI 304 by the SiC ball and its monitoring via Barkhausen noise emission.* Wear, 204492.

[29] Peng, Y., & Huang, H. (2022). *Mechanical and magnetic properties of TRIP690 steel strengthened by strain-induced martensite*. Journal of Magnetism and Magnetic Materials, 550, 169083.

[30] Neyra Astudillo, M. R., Núñez, N. M., López Pumarega, M. I., Ferrari, G., Ruzzante, J., & Gómez, M. (2022). *Study of martensite induced by deformation with Magnetic Barkhausen Noise technique*. Journal of Magnetism and Magnetic Materials, 556, 169454.

[31] Mészáros, I., & Prohászka, J. (2005). *Magnetic investigation of the effect of α'-martensite on the properties of austenitic stainless steel.* Journal of Materials Processing Technology, 161(1-2), 162–168.

[32] Tian, Y., Borgenstam, A., & Hedström, P. (2018*). Comparing the deformation-induced martensitic transformation with the athermal martensitic transformation in Fe-Cr-Ni alloys*. Journal of Alloys and Compounds, 766, 131–139.

[33] Pulagam, S. S. R., & Dutta, A. (2022). *Peierls–Nabarro modeling of twinning dislocations in fcc metals*. Computational Materials Science, 206, 111269.

[34] Li, X., Schönecker, S., Vitos, L., & Li, X. (2022). *Generalized stacking faults energies of face-centered cubic high-entropy alloys: A first-principles study*. Intermetallics, 145, 107556.

[35] Neslušan, M., Minárik, P., Čep, R., Uríček, J., Trojan, K., Ganev, N., & Trško, L. (2022). *Barkhausen noise emission of AISI 304 stainless steel originating from strain induced martensite by shot peening*. Journal of Materials Research and Technology.

[36] Jančárik, V., Palček, P., & Hilko, K. (2021). *Magnetic testing of ferritic stainless steel*. In applied physics of condensed matter (APCOM 2021). AIP Publishing.

[37] Sendrowicz, A., Myhre, A. O., Danyuk, A. V., & Vinogradov, A. (2022). *Dislocation kinetics explains energy partitioning during strain hardening: Model and experimental validation by infrared thermography and acoustic emission.* Materials Science and Engineering: A, 143969.

[38] Durand-Charre, M. (2013). *Microstructure of Steels and Cast Irons*. Springer Science & Business Media.

[39] Tian, Y. Z., Zhao, L. J., Chen, S., Shibata, A., Zhang, Z. F., & Tsuji, N. (2015). *Significant contribution of stacking faults to the strain hardening behavior of Cu-15%Al alloy with different grain sizes.* Scientific Reports, 5(1).

[40] Lu, J., Hultman, L., Holmström, E., Antonsson, K. H., Grehk, M., Li, W., Vitos, L., & Golpayegani, A. (2016). *Stacking fault energies in austenitic stainless steels*. Acta Materialia, 111, 39–46.

[41] Asgari, S., El-Danaf, E., Kalidindi, S. R., & Doherty, R. D. (1997). *Strain hardening regimes and microstructural evolution during large strain compression of low stacking fault energy fcc alloys that form deformation twins.* Metallurgical and Materials Transactions A, 28(9), 1781–1795.

[42] Shen, Y. F., Li, X. X., Sun, X., Wang, Y. D., & Zuo, L. (2012). *Twinning and martensite in a 304 austenitic stainless steel.* Materials Science and Engineering: A, 552, 514–522.

[43] www.helmut-fischer.com

[44] Gubbels, W. *Barkhausen Noise NDI for Heat-Treatment Defects and Case-Depth Analysis.* Online article, Industrial Heating.